Senescence-specific translation dysregulation desensitizes cells to stress by inhibiting activation of the integrated stress response

Matthew J. Payea[$], Showkat A. Dar, Carlos Anerillas, Jennifer L. Martindale, Cedric Belair, Rachel Munk, Sulochan Malla, Jinshui Fan, Yulan Piao, Xiaoling Yang, Abid Rehman, Nirad Banskota, Kotb Abdelmohsen, Myriam Gorospe, Manolis Maragkakis[$]

Laboratory of Genetics and Genomics, National Institute on Aging, Intramural Research Program, National Institutes of Health, Baltimore, MD 21224, USA

[$] To whom correspondence should be addressed

Contact: maragkakis@nih.gov

Abstract

Senescence is a state of indefinite cell cycle arrest associated with aging, cancer, and age-related diseases. Here, using label-based mass spectrometry, ribosome profiling and nanopore direct RNA sequencing, we explore the coordinated interaction of translational and transcriptional programs of human cellular senescence. We find that translational deregulation and a corresponding maladaptive integrated stress response (ISR) is a hallmark of senescence that desensitizes senescent cells to stress. We show that senescent cells maintain high levels of eIF2α phosphorylation, typical of ISR activation, but translationally repress the stress response transcription factor 4 (ATF4) by ineffective bypass of the inhibitory upstream open reading frames. Surprisingly, ATF4 translation remains inhibited even after acute proteotoxic and amino acid starvation stressors, resulting in a highly diminished stress response. Furthermore, absent a response, stress exacerbates the senescence secretory phenotype and inflammatory pathways thus acting as a possible mechanistic link to disease. Our results reveal a novel mechanism that senescent cells exploit to evade an adaptive stress response and remain viable.

Introduction

Cellular senescence is a state of virtually permanent cell cycle arrest that typically occurs in response to sublethal genomic damage. Senescence is expected to primarily guard against carcinogenesis by forcing cells with potentially tumorigenic mutations out of the cell cycle[1,2], though other functions for senescence in development[3] and wound healing[4,5] have also been described. However, senescent cells are also detrimental to human health as their prevalence increases during aging[6] and their accumulation is linked to several diseases [7-9]. The detrimental trait of senescent cells on organismal health is primarily attributed to the senescence associated secretory phenotype (SASP), which describes the dramatic increase in secretion of interleukins, cytokines, and other proteins[10-14]. The link between senescence and age-related diseases has been further established by advancements in senolytics, a class of senescent-specific cytotoxic drugs, that have been used to show that selective clearance of senescent cells is associated with improvements in health[15-17]. Thus, there is a growing appreciation for a seno-centric framework of aging[18], in which senolytic therapies can serve a unified approach for aging intervention[19-23].

Since senolytics would primarily serve as quality-of-life therapies, it is important to identify senescence-specific changes to cellular function that can be exploited for maximum selectivity. The current knowledge on the biology of senescence benefits from high-throughput analyses that have established several key components of the senescent transcriptome and secretome[11,12,24,25], but comparatively less is known about the senescent proteome[26-28] and the involved translation regulatory mechanisms[29].

Here we coupled Tandem-Mass Tag (TMT) mass spectrometry, ribosome profiling, and full-length, direct RNA nanopore sequencing (dRNA-Seq) in senescent, quiescent, and cycling states to discover senescence-specific regulation of translation and the proteome that directly dictates cell survival and secretory programs in human cellular senescence. Our analysis identified that senescent cells possess unique increases in ER stress proteins, decreased spliceosome proteins, and a global reduction in translating ribosomes. Interestingly, they also display a stable increase in eIF2α phosphorylation, a critical integrated stress response (ISR) marker, surprisingly without downstream induction of the key ISR transcription factor ATF4.

We determined that this resistance to ATF4 expression in senescence is a consequence of the decreased competition for ternary complex due to a widespread decrease in translation that leads to inefficient ribosome bypass of upstream Open Reading Frames (uORF) in ATF4. Consequently, we find that the reduced efficacy of ATF4 expression causes senescent cells to be globally resistant to ISR activation under both proteotoxic stress and amino acid starvation. Surprisingly, senescent cells maintain increased eIF2α-P even 20h after stress has been removed, accompanied by a durable transcriptional increase in several inflammatory proteins. Our work provides the most complete profiling of the intersection between transcriptome, translatome, and proteome for senescence, and identifies a fundamental cellular mechanism that confers resistance to stress response.

Results

Cellular senescence is characterized by persistent ER stress signaling but post-transcriptional inhibition of ATF4 activation

To perform a direct and quantitative comparison of the senescent, cycling, and quiescent proteomes, we used TMT isobaric labeling and mass spectrometry using IMR-90 human lung fibroblasts. We chose a DNA-damage induced model of senescence for study, which was generated through treatment of cells with the topoisomerase II inhibitor etoposide as previously described [30,31]. Senescent cells were compared to both young dividing cells (Cyc) and contact-inhibited quiescent cells (Qui), to control for changes associated with general cell cycle arrest. We validated the senescence phenotype of Etop cells using a multi-marker workflow[32]. As expected, western blot analysis indicated Etop cells had increased expression of cell-cycle inhibitors ($p16^{INK4A}$, $p21^{CIP1}$) and decreased expression of LMNB1 **(Fig. 1A)**. Similarly, RT-qPCR analysis showed increased expression of *CDKN1A* ($p21^{CIP1}$) and the SASP factor *CXCL8* **(Fig. 1B)**. Senescent cells also showed high positivity in a senescence-associated β-galactosidase activity (SA-βGal) assay compared to cycling cells, further confirming the senescence phenotype **(Fig. 1C, Fig. S1A)**.

Whole-cell protein lysates from the Etop, Cyc, and Qui cells were harvested in biological triplicate, processed for TMT-multiplex labeling, fractionated, and then analyzed by LC/MS/MS. We identified 6,254 proteins across all 9 libraries after filtering **(Table S1, see methods)**.

Principal component analysis (PCA) showed that the proteomes of Cyc, Qui, and Etop cells were highly distinct whereas replicates were closely associated **(Fig. S1B)**. We performed differential protein expression analysis for Etop/Cyc and Etop/Qui comparisons and defined a threshold for significant biological change that was retrospectively determined to be at least ~2-fold by western blot analysis **(Fig. S1C, see methods)**. Our analysis identified several proteins with substantial change in both comparisons, including expected changes in the senescence markers relative to both Cyc and Qui cells **(Fig.1D, Fig. S1D)**.

To identify robust protein expression changes that were unique to the senescence state, we selected for proteins that were significantly changed in Etop compared to both Cyc and Qui cells. This revealed 866 proteins that were uniquely decreased in senescence and 1,112 that were uniquely increased **(Fig. 1E, Table S1)**. Gene Set Enrichment Analysis (GSEA)[33] identified several trends associated with previously established senescence phenotypes[1,32], as well as two novel and significant areas of senescence-specific change: suppression of mRNA splicing and activation of endoplasmic reticulum (ER) proteins **(Fig. 1F, Fig. S1E)**. Further enrichment analysis with the Kyoto Encyclopedia of Genes and Genomes (KEGG)[34] confirmed the spliceosome and ER processing pathways as areas of strong regulation **(Fig. S1F,G)**, suggesting that changes in both of these processes may be hallmarks of senescence.

Notably, we observed increases in PERK (eIF2AK3) **(Fig. S1F)**, an ER stress sensing kinase that phosphorylates the translation initiation factor eIF2α (eIF2α-P) to both reduce protein synthesis and promote expression of the multi-functional transcription factor ATF4 [20]. We therefore measured eIF2α-P and ATF4 levels to test whether the ISR and unfolded protein response (UPR), which co-activate to resolve proteotoxic stress, were basally activated in senescent cells. We used Etop cells and an additional DNA-damage induced senescent model: ionizing radiation induced (IR) senescence. As a reference for ER stress, we compared Etop and IR cells to cells treated with the ER stress inducer thapsigargin (Tg)[35], referred to as CTg cells hereafter**.** Etop and IR cells had distinctive increases in eIF2α-P, which were highly reproducible and similar in magnitude to CTg cells. However, in contrast to CTg, we found that surprisingly neither Etop nor IR cells expressed ATF4 **(Fig. 1G,1H)**. RT-qPCR analysis showed no reduction in *ATF4* mRNA in senescence compared to Cyc cells contrary to what has been previously described for UV treated cells [36,37] **(Fig. S1H)**, which indicated ATF4 was likely suppressed by an unknown post-transcriptional mechanism.

Since the senescence phenotype has been observed to have high heterogeneity with respect to both method of induction and cell type [11,24,25] we examined whether increased eIF2α-P without ATF4 expression was generalizable to other models. We found that Etop treatment of WI-38 lung fibroblasts, BJ foreskin fibroblasts, and HUVEC vein endothelial cells produced similar increases in eIF2α-P without ATF4 expression **(Fig. S1I)**. Similarly, we saw that replicative exhaustion of IMR-90 cells also produced the same phenotype **(Fig. S1J)**. The induction of senescence occurs in phases [31,38] and so we tested whether ATF4 was expressed earlier during the establishment of senescence. Interestingly, we found that while eIF2α-P levels steadily increased over time, ATF4 expression only briefly increased at induction but reduced shortly after **(Fig. 1I).** Thus, our results show that senescence is generally associated with a continual source of ER stress that chronically induces eIF2α-P but with a progressive insensitivity to it that limits induction of ATF4 post-transcriptionally.

128 **Ribosome uORF bypass is not activated in senescent cells**
129 Phosphorylation of eIF2α in the ISR serves primarily to limit availability of the ternary complex
130 (eIF2α-GTP-$tRNA_i^{Met}$), which results in decreased translation initiation and increased 40S
131 ribosomal subunit scanning [20]. Therefore, while increased eIF2α-P levels decrease translation
132 globally, they also promote ribosome bypass of an inhibitory upstream open reading frame
133 (uORF) in favor of the main ATF4 ORF. The disconnect between eIF2α-P levels and ATF4
134 protein expression suggested that eIF2α-P was not sufficiently limiting the ternary complex
135 availability for uORF bypass in senescence.

136 To test this hypothesis, we performed polysome profiling to probe the translational status
137 of ATF4 mRNA. We performed polysome profiling on Cyc, Etop, IR, and CTg cells, and found
138 that both Etop and IR cells had profiles that strongly resembled that of CTg cells consistent with
139 ISR activation, with a characteristic increase in non-translating monosomes and decrease in
140 translating polysomes **(Fig. 2A)**. RT-qPCR analysis of our polysome profiling fractions showed
141 that *ATF4* mRNA was predominantly in the non-translating monosome fraction of senescent and
142 Cyc cells, while CTg cells showed a clear shift toward the polysomes **(Fig. 2B)**. This result
143 shows that the ATF4 mRNA is not engaged with ribosomes as would have been expected under
144 high eIF2α-P levels that would permit uORF bypass, We further tested the contribution of eIF2α-
145 P in senescence by treating cells with the ISR inhibitor (ISRIB) drug, which suppresses the
146 effects of eIF2α-P on translation. Treatment of CTg cells with ISRIB produced a substantial
147 reduction in monosome accumulation but showed very little effect on Etop cells **(Fig. S2A)**, thus
148 showing that eIF2α-P has little effect on translation in senescence.

149 To further test the translation dynamics on ATF4 and to globally assess why eIF2α-P
150 may not be functioning as expected in senescence, we performed ribosome sequencing (Ribo-
151 Seq) of Etop, IR, Qui, and Cyc cells and coupled that with RNA sequencing (RNA-seq)
152 measured in parallel from a single lysate. We calculated translation efficiency by quantifying
153 ribosome footprints relative to mRNA levels as previously described [40]. We found good
154 correlation between replicates of each condition in both the Ribo-Seq and RNA-seq libraries
155 **(Table S2, Fig. S2B)**. PCA showed that Etop and IR datasets were closely associated while
156 also being distinct from the Cyc and Qui conditions **(Fig. S2C)**. Differential RNA-seq analysis
157 captured several markers of senescence as previously described [24,25], and confirmed our finding
158 that *ATF4* mRNA levels are not substantially changed in senescence relative to Cyc cells **(Fig.
159 2C, Table S2).** Similarly, GSEA identified gene expression patterns frequently ascribed to the
160 senescence phenotype **(Fig. S2D**). We next identified transcripts with detectable changes to
161 translational efficiency relative to Cyc cells. We found that both Etop and IR cells had very few
162 genes (25 and 29 genes, respectively) with a statistically significant (adjusted p-value ≤ 0.05)
163 change in translation efficiency, though both were greater than what was observed in Qui cells
164 (5 genes) **(Fig. 2C, Fig. S2E)**. Consistent with our western and polysome analysis, we found no
165 significant difference in the translation efficiency of *ATF4* in either of the four conditions **(Table
166 S2)**. Further examination of ribosome footprint distribution on *ATF4* mRNA showed that
167 ribosomes were predominantly located in the uORFs rather than in the coding region for Etop
168 and IR cells **(Fig. 2D).** These results confirmed that senescent cells were not permitting uORF
169 bypass for ATF4 despite elevated eIF2α-P.

170 **Global decrease in translating ribosomes inhibits the ISR in senescence**
171 The lack of uORF bypass we observed in senescence indicated that eIF2α-P levels were
172 not effectively increasing 40S scanning. We considered senescent cells may have a separate

173 global translational change that suppressed the effects of eIF2α-P, and which would not be
174 easily detectable from measurements of translation efficiency. To test this we performed
175 metagene analysis to identify potential changes in the distribution of ribosome footprints along
176 mRNAs. We found that senescent cells possessed a minor bias toward the 5' end of the coding
177 sequence (CDS) compared to Cyc and Qui cells (middle panel) and were nearly identical in the
178 5' UTR and 3' UTR regions **(Fig. 3A)**. Similarly the overall ribosome footprint distribution within
179 1000 nts of the start site did not indicate any substantial change between our libraries. However,
180 senescent cells had far less reads in total over the same window **(Fig. 3B, Fig. S3A)**,
181 suggesting fewer translating ribosomes in total during senescence. Indeed, after normalizing for
182 RPKM, we found that the ratio of Ribo-seq/RNA-seq reads for both Etop and IR cells was
183 substantially less compared to both Cyc and Qui cells **(Fig. 3C, Table S2**, see methods**)**. Linear
184 regression analysis further showed that senescent cells had ~4 times less ribosomes per unit of
185 RNA compared to either Cyc or Qui cells **(Fig. 3D)**.

186 Our ribosome sequencing data thus strongly suggested that there were fewer translating
187 ribosomes in senescent cells, indicating dramatic decreases in senescent translation machinery.
188 A search of translation factors within our mass spectrometry dataset identified several as
189 uniquely decreased in senescence **(Table S2)**. Most impressively, ribosomal proteins
190 experienced a statistically significant (p-value ≤ 0.05) group-wide reduction in both the Etop/Cyc
191 and Etop/Qui comparisons **(Fig. 3E)**. Decreased ribosomal proteins were consistent with the
192 reduction in ribosome footprints we observed, as well as broad decreases in rRNA biogenesis in
193 senescence [41,42]. Our results predict that senescent cells would have markedly reduced total
194 protein synthesis which we verified by measuring the rate of nascent protein production after
195 pulsing with a methionine analogue. We found that both Etop and IR cells produced far less
196 protein (green signal) over a 60-minute interval compared to Cyc cells **(Fig. 3F, S3B)**,
197 consistent with a senescence-associated global decrease in translating ribosomes.

198 A reduction in translating ribosomes presented a mechanistic explanation for why the
199 uORF bypass of ATF4 would be ineffective in senescence. ATF4 expression depends on the
200 dynamic balance of ternary complex availability and ribosome demand to initiate translation.
201 Under high ribosome load and reduced ternary complex availability, 40S scanning through the
202 inhibitory uORF is promoted. However, under a senescence-associated ribosome decrease, the
203 ternary complex availability would effectively appear increased, thus suppressing 40S scanning.
204 In fact, previous work has suggested that the eIF2α pool is typically used at capacity in cells[43],
205 and while our data show decrease in ribosome footprints and ribosomal proteins, we observed
206 no change in eIF2α protein expression **(Table S1)**, indicating it is at excess of translation during
207 senescence. A core prediction of our model is that senescent cells should be capable of
208 expressing ATF4 if the inhibitory uORF is removed. We tested this by generating constructs with
209 ATF4 downstream of a T7 promoter using intact (WT), missense mutation carrying (ΔuORF),
210 and 5' UTR shortened past uORFs (Mut) **(Fig. 3G)**. As predicted by our model, we found that
211 transfection of WT *ATF4* produced very little protein expression, while ΔuORF produced
212 substantially more **(Fig. 3H)**. Transfection of the Short-*ATF4* construct resulted in even further
213 increase **(Fig. 3I)**, possibly due to elimination of uORF0 that we had observed a substantial
214 amount of ribosome footprint density on **(Fig. 2D)**. Collectively, our data show that senescent
215 cells have fewer translating ribosomes and that this causes decreased uORF bypass with direct
216 consequences for ATF4 translation inhibition and the ISR.

217

Senescent cells fail to activate the ISR in response to acute stress

Our model also suggested that senescent cells would be less responsive to additional stressors registered by the ISR. We thus compared the ability of senescent, cycling, and quiescent cells to express ATF4 after acute proteotoxic and oxidative stress through treatment with Tg and sodium arsenite (Ars), respectively. We found that while treatment of Cyc and Qui cells with either stressor induced a strong increase, Etop cells showed substantial resistance to ATF4 expression despite higher than Cyc and Qui cells eIF2α-P levels **(Fig. 4A)**. We next tested whether the kinetics of ISR activation had changed in senescence. Treatment of Cyc cells with Tg produced a rapid increase in eIF2α-P and concurrent ATF4 protein expression, which was suppressed by addition of the eIF2AK3 inhibitor GSK2656157[44] **(Fig. 4B, Fig. S4A).** Conversely, Tg treatment of both Etop and IR cells again elicited a far weaker expression of ATF4, despite substantial increases in eIF2α-P **(Fig. 4B, Fig. S4A)**. Quantification of the ATF4/eIF2α-P signal ratio showed that Etop cells were ~7 times less effective at inducing ATF4 expression compared to Cyc cells, despite similar levels of *ATF4* mRNA **(Fig. S4B)**, consistent with our model of an increased eIF2α-P threshold for the ISR in senescent cells.

Our initial screen with Tg and Ars suggested that general cell cycle arrest was not sufficient to cause ISR restriction as Qui cells were able to produce ATF4 in response to Tg and Ars. We additionally compared Tg treatment of Etop, Cyc, and serum-starved quiescent cells and again found that senescent cells were uniquely resistant to expression of ATF4 **(Fig. S4C)**. Previous studies have shown that cells induced to senescence through replicative exhaustion are resistant to the UPR[23] and so we tested whether the UPR would be similarly inactive for Etop cells treated with Tg. In fact, we observed a complete absence of mature Xbp1 and ATF6 UPR transcription factors [45] in Tg treated Etop cells **(Fig. S4D)**, indicating a general senescence-specific restriction in the stress response.

Our results indicated that while senescent cells possess elevated eIF2α-P, they do not activate the downstream transcriptional program of the ISR or UPR. To comprehensively test this, we performed full-length, long-read direct RNA sequencing (dRNA-seq)[46] of Cyc, Etop, ETg, and CTg cells **(Table S3)**. Our data were highly reproducible across replicates **(Fig. S4E)** and allowed the simultaneous quantification of the abundance and splicing status of the senescence transcriptome at single-molecule resolution. To our knowledge, there have been no previous analyses of senescent cells using nanopore based sequencing technology and so we first performed differential expression analysis between untreated Etop and Cyc cells. Overall, we quantified 8,587 expressed genes **(Table S3, see methods)**, 271 of which showed statistically significant (adjusted p-value ≤ 0.05) mRNA abundance changes of at least 2-fold, including several senescent markers [24,25,32]**(Fig. 4C, Fig. S4F)**. Long-read sequencing also allowed us to interrogate features of the mRNAs that are not typically captured in short read RNA-Seq such differences in 5' end degradation and poly-A tail deadenylation that may indicate changes in mRNA decay[46]. Our data showed little significant change (q-value ≤ 0.05) between Cyc and Etop cells in both features, though we did note a minor trend toward shortened 5' ends in senescence at a lower threshold of significance **(Fig. S4G)**.

We next interrogated the expression of previously identified targets of the ISR and UPR[21,47,48] in the Etop/Cyc and CTg/Cyc comparisons. As predicted, we found that while CTg cells displayed 2-fold increases in several of these genes, only few of them were elevated in Etop cells **(Fig. 4D)**. We further examined whether senescent cells would undergo transcriptional changes after Tg treatment. We found that while ETg cells did increase expression over ETop for some of these ISR/UPR genes, the response was highly diminished

compared to CTg cells **(Fig. 4E)**, strongly suggesting that the inefficiency of ATF4 expression is indicative of a decreased transcriptional response.

We also tested whether senescent cells would be able to trigger the ISR in response to a different stressor: starvation of amino acids. We grew Cyc and Etop cells in media lacking the amino acids methionine and cysteine (-Met -Cys) and supplemented with dialyzed FBS, which lacks amino acids, to maintain growth rate and accelerate amino acid starvation. We found that senescent cells produced no detectable ATF4 protein even after five hours of amino acid starvation, in stark contrast to Cyc cells that responded within 1h **(Fig. 4F).** This resistance to starvation was independent of amino acid composition, as starvation of lysine and arginine (-Lys -Arg) in Etop and Cyc cells produced similar results **(Fig. 4G)**. Furthermore, we found that resistance to ATF4 expression extended to IR cells **(Fig. S4H)** but was not present in Qui cells **(Fig. S4I)**, arguing that the lack of starvation response was a function of senescence and not general to cell cycle arrest.

We again used dRNA-seq to analyze mRNA changes between Etop and Cyc libraries to cells starved of methionine and cysteine (ESv, CSv) **(Table S3)**. As with the response to ER stress, we evaluated the starvation response in ESv and CSv cells by looking for mRNA increases in genes previously identified as upregulated by starvation[49]. We saw that CSv cells produced increases in the greatest number of starvation targets **(Fig S4J)**. Combined, our data strongly suggest that senescent cells are generally resistant to activation of stress response pathways at both the proteomic and transcriptomic level even when challenged by additional stress.

Unresolved acute stress enhances the senescence associated secretory phenotype

While senescent cells did not activate the ISR in response to stress, we did observe a senescence-specific increase in several transcripts, many of which in inflammatory pathways **(Fig. 5A)**. The senescence associated secretory phenotype (SASP) is a senescence hallmark and describes the substantial secretion of cytokines, interleukins, and other proteins by senescent cells [10,11,13]. Several SASP factors have also been associated with ER stress in different contexts [50-52] and we thus considered that while senescent cells do not effectively activate the ISR, stress may still increase SASP factor production.

To identify stress-induced increases comprehensively, we identified genes from our dRNA-seq data that were elevated after stress in Etop cells but not Cyc cells **(Table S3).** KEGG analysis confirmed that these genes were predominantly associated with inflammatory and secretory pathways **(Fig. 5B)**. Though the SASP includes several proteins not typically associated with secretion[11], we further refined our gene list to those annotated in the predicted secretome from the protein atlas [53]. We found 21 secretory protein genes among the stress-enhanced genes, including several well-established SASP factors **(Fig. 5C)**. Thus, our data indicate that while senescent cells do not effectively activate the ISR, they do transcriptionally enhance elements of the SASP during both proteotoxic and starvation stress.

In normal cells, activation of the ISR is followed by a recovery period after the initial stress has been resolved. This partly involves the action of the phosphatase GADD34 (PPP1R15A) that dephosphorylates eIF2α both to enable the translation of the upregulated factors and to begin the reduction of ATF4 expression[20]. In addition to PPP1R15A being a transcriptional target of ATF4, its translation is regulated using a similar inhibitory uORF mechanism[39]. Our model for deficient uORF bypass thus predicts that senescent cells would be unable to effectively express PPP1R15A. In fact, western blot analysis showed that PPP1R15A

309 was inefficiently expressed during senescence even after treatment with Tg **(Fig. 5D)**. This
310 suggested that, in addition to being ineffective at increasing ATF4 protein levels, senescent cells
311 may be unable to reduce the levels of eIF2α-P after stress. To test this, we treated Etop and
312 Cyc cells with Tg for 3h, then changed the media and allowed cells to recover for an additional
313 20 hours in optimal growth conditions. Western blot analysis showed that the stressed Etop
314 cells had marked increases in eIF2α-P compared to the untreated Etop cells, though neither
315 condition showed enduring ATF4 expression **(Fig. 5E)**. Interestingly, RT-qPCR analysis showed
316 that the stress-enhanced transcriptome also lasted beyond the original stress, particularly for
317 tested SASP factors **(Fig. 5F)**. Thus, our results show that not only does stress enhance the
318 senescent phenotype, but enhancement persists beyond the initial stress and optimal growth
319 conditions are not sufficient to repair it.

320 Discussion

321 Senescence has been identified to serve multiple functions in organisms, from development to
322 wound healing[32], but is primarily expected to serve as a guard against tumorigenesis induced
323 through sub-lethal genomic damage. As such, senescence can be viewed as a stress response,
324 since it detects a stress and then induces an intense transcriptomic and proteomic remodeling
325 for adaptation [31,38,54]. The PCA for our dRNA-seq libraries point toward this same conclusion,
326 wherein the first principal component appears to describe stress and places senescence as a
327 more stressful state than exposure to either metabolic or proteotoxic stress **(Fig. 6A)**. However,
328 unlike the ISR, which functions to eventually restore homeostasis, senescence operates as a
329 terminal stress response by converting damaged cells to an entirely new state with its own
330 unique set of stable phenotypes**.** Thus, while principally like other stress responses, senescence
331 has an entirely novel set of demands in its adaptive program, namely, to prepare for indefinite
332 survival with unresolved cellular damage.

333 A defining feature of this framework is to achieve maximum survivability with minimal
334 change, and thus avoidance of the ISR, even during stress. Our data show that the availability
335 of translating ribosomes is a key determinant of senescent cells resistance to the ISR, and by
336 extension to any stress response that requires proteomic remodeling. Even apoptosis, which
337 senescent cells have long been understood to resist, would require substantial translational
338 effort that our results show senescent cells appear to be intrinsically resistant to. A link between
339 ribosome content and the efficacy of stress responses poses far-reaching implications to other
340 conditions where ribosomes are dramatically decreased, such as ribosomopathies like
341 Diamond-Blackfan anemia[55].

342 The mechanism by which translating ribosomes are depleted in senescence may be due to a
343 variety of sources. Senescent cells expand in size which may dilute the ability of ribosomes to
344 adequately initiate[56] and senescence has also been associated with decreases in rRNA
345 transcription and maturation[41,42]. Interestingly, in addition to decreases in ribosomal proteins,
346 our long-read sequencing data showed that ribosomal proteins frequently had increases in
347 alternative splicing in senescence **(Fig. 6B)**, though the contributions to protein levels are
348 unclear. It is also possible that, rather than a reduction in absolute ribosome content, translation
349 slows due to an accumulation of inactive 80S monosomes, which are stable but not bound to
350 mRNA, and have been shown to arise in several conditions[57-59]. However, while the decrease in
351 translating ribosomes is a defining difference between cycling and senescent cells, quiescent
352 cells also reduce their translation capacity and have a similar aim to survive under sub-optimal

353 conditions indefinitely. In fact, quiescence and senescence have several areas of commonality
354 including the nature of their cell cycle arrest [60] and in the regulation of inflammatory genes by
355 p38 MAPK-MK2 signaling [61-63]. We further see that quiescent and senescent cells displayed
356 high similarity in polysome profiling, further indicating a common translational arrest. What
357 separates them in our work, is that neither contact-inhibition or serum-starvation induced
358 quiescent cells show resistance to ISR activation as senescence.

359 The difference between quiescent and senescent cells may then be the degree of
360 translational arrest that occurs. While quiescence is intended to be temporary and must
361 therefore re-engage in the translationally expensive process of cell division, senescence is
362 expected to be a terminal fate and so the translational capacity can be reduced to the minimum.
363 Our results suggest that cell states can thus be modeled as a dynamic continuum of ribosome
364 and ternary complex availability, wherein greater translation coincides with reduced ternary
365 complex availability, which in turn increases stress sensitivity **(Fig. 6C)**. One important question
366 that arises from such a model is how these states are maintained and whether ribosome content
367 is the cause or consequence of their induction. Future work will be needed to address how
368 much of the senescence phenotype can be explained by decreased translation as well as
369 understanding whether a restrictive translation environment poses liability to senescence that
370 can be exploited therapeutically. Furthermore, since senescent cells are long-lasting and likely
371 experience several rounds of stress, the way in which they cope with stress in the absence of
372 stress responses will have important implications for aging.

373 Methods

374 Cell culture

375 IMR-90 human lung fibroblasts (Coriell Institute) were cultured in high-glucose DMEM (Gibco)
376 supplemented with 10% heat-inactivated FBS (Gibco), nonessential amino acids (1x, Gibco),
377 and antibiotic/antimycotic mix (1x, Gibco). Cells at ~40-60% confluency and at a population
378 doubling level (PDL) between 20-30 were considered Cycling (Cyc). Contact-Inhibited
379 Quiescent cells (Qui) were prepared essentially as described[64] by allowing Cyc cells to reach
380 ~100% confluency and growing for an additional four days, changing media every 2 days and
381 24 hours before harvest. Etoposide-induced senescent (Etop) cells were prepared by treating
382 Cyc cells with 50 μM etoposide (Selleckchem, dissolved in DMSO) over 10 days (treatments on
383 day 0, day 2, and day 4) with media changed every two days. Ionizing-radiation induced
384 senescent (IR) cells were generated as described [65] by exposing Cyc cells to 15 grays of
385 ionizing radiation from a cesium-137 irradiator (Nordion) and then culturing for 10 days with
386 media changed every two days. Cells were harvested by trypsinization using TrypLE
387 (ThermoFisher Scientific), pelleted at 4ºC for 5 minutes at 600 x g and washed once in PBS
388 before generation of protein lysates or bulk RNA as described below.

389 Senescence validation

390 Senescence was validated using at least one of four methods: SA-β-Gal staining as per
391 manufacturer's instructions (Cell Signaling Technology), determination of cell cycle arrest using
392 an EdU incorporation assay (ThermoFisher Scientific) as per manufacturer's instructions,
393 measurement of senescence associated protein markers (increased $p16^{INK4A}$ and $p21^{CIP1}$,
394 decreased LMNB1), and elevated SASP factors measured by RT-qPCR (*CXCL8*, *IL6*, *CCL2*).

395 Tandem Mass Tag mass spectrometry preparation and data analysis

396 Cyc, Qui, and Etop cells prepared as described were harvested by generating cell pellets
397 through trypsinization and resuspended in mass spec buffer (100 mM Tris, 150 mM NaCL, 4%
398 SDS, 1% Triton X-114, 0.1M DTT, and 1X Halt Protease Cocktail (Sigma) followed by
399 sonication for 2.5 minutes and denaturation at 95ºC for 3 minutes. Lysates were submitted for
400 processing and analysis to Poochon Scientific (Frederick,MD) for quantitative proteomics using
401 trypsin digestion, TMT-16plex labeling, fractionation by reverse-phase UHPLC, and LC-MS/MS
402 analysis. Processed mass spectrometry data are available in **Table S1**.

403 Data was analyzed and volcano plots were generated using R data analysis software. Mass
404 spectrometry data was filtered for proteins assigned with "medium" or "high" confidence at
405 detection, as well as for proteins that showed a coefficient of variation ≤ 0.15 among biological
406 triplicates. After filtering, principal component analysis was performed using base R function
407 with all 9 sample libraries as the input. Biologically relevant protein changes were arbitrarily
408 assigned to a $\log_2$ fold-change (log2FC) of 0.2/-0.2 and p-values ≤ 0.05 by two-tailed student's
409 T-test (Etop vs. Cyc, or Etop vs. Qui). GSEA analysis was performed on proteins identified as
410 having at least 0.2/-0.2 log2FC in both the Etop/Cyc and Etop/Qui comparisons using the
411 ClusterProfiler package[33].

412 **Western blot and RT-qPCR analysis**
413 Protein lysates for western blot analysis were extracted from cell pellets (≤ 2 x 10^6 cells) using
414 100 uL lysis buffer (2% SDS 50 mM HEPES) followed by water bath sonication and
415 denaturation at 95ºC for 3 minutes. Lysates were quantified using a BCA protein assay kit
416 (ThermoFisher Scientific) and then equal amounts of protein were loaded onto a 4-20% SDS-
417 PAGE gel (Biorad) and then transferred to a nitrocellulose membrane (BioRad). Western blot
418 analysis was performed using the iBind system (ThermoFisher Scientific) as described by the
419 manufacturer and with antibodies and amounts listed in Table S4. Quantification of western
420 blots was performed in Image Lab (BioRad). Antibodies and dilutions used in this study listed in
421 **Table S4**.

422 Bulk-RNA free of genomic DNA for RT-qPCR analysis was extracted from cell pellets (≤ 2 x 10^6
423 cells) using the RNeasy plus spin-column purification kit (Qiagen) and performed using the
424 Qiacube liquid handler (Qiagen) as described by the manufacturer. Extracted RNA was then
425 amplified using Maxima reverse transcriptase (ThermoFisher Scientific) and random hexamer
426 primer. cDNA was then analyzed using two-step RT-qPCR using SYBR Green mix (Kappa
427 biosystems) and analyzed using the $2^{-\Delta\Delta CT}$ method. Primers used are listed in **Table S4**.

428 **Ribosome Sequencing Library Preparation**
429 IMR90 cell prepared as described above for Cyc, Qui, IR, and Etop conditions were harvested
430 by transfer to ice and washing once with ice-cold 0.1 mg/mL cycloheximide in PBS. After
431 supernatant was removed completely, cells were lysed by adding 500 uL ice-cold polysome
432 lysis buffer (20 mM Tris pH 7.5, 50 mM NaCl, 1 mM DTT, 50 mM KCl, 1% Triton x-100, 0.1
433 mg/mL cycloheximide, and 1x HALT protease phosphatase inhibitor cocktail (ThermoFisher
434 Scientific)) dropwise. Lysates were scrapped and then triturated 3x through a 26g needle
435 followed by centrifugation at 18k x g at 4ºC for 10 min. RNA content was approximated by
436 nanodrop OD 260 units and 50 ug was aliquoted for RNA-sequencing and Ribo-sequencing for
437 each biological replicate.

438 Ribo-seq lysates were treated with 1 uL of RNAseq 1 (ThermoFisher Scientific) at 4ºC for 40
439 minutes with shaking and reaction was stopped by addition of 200 U SUPERaseIN

(ThermoFisher Scientific). Digested lysates were then overlaid on 900 uL of a 1M sucrose cushion in a 13 x 51 mm polycarbonate tube (Beckman Coulter), followed by ultracentrifugation at 70k RPM at 4ºC for 2 h (Optima TLX ultracentrifuge, Beckman Coulter). Ribosome pellets were then resuspended in Trizol and extracted for RNA according to manufacturer's instructions. Extracted RNA was then subjected to DNAse I treatment for 15 minutes at 37ºC and then subjected to gel purification on a 15% polyacrylamide TBE-urea gel to isolate ribosome footprints. Isolated footprints were extracted from gel slices using extraction buffer (300 nM NaOAc pH 5.5, 1 mM EDTA, 0.25% SDS) overnight at room temperature followed by isopropanol precipitation. Precipitated footprints were depleted of rRNA using Low Input RiboMinus Eukaryote System v2 kit (ThermoFisher Scientific) and then subjected to end healing using T4 PNK (New England BioLabs). Resulting footprints were then used to generate sequencing libraries using the NEBNext Small RNA Library Prep Set for Illumina kit (New England BioLabs). Library quality was assessed using High Sensitivity DNA Chips with the Agilent 2100 Bioanalyzer System (Agilent Technologies).

RNA-seq lysates were extracted for bulk RNA in Trizol according to manufacturer's instructions. RNA quality was assessed using a TapeStation analyzer (Agilent Technologies) and only RNA integrity numbers (RIN) greater than 9 were chose for further library preparation. Libraries were prepared with the TruSeq Stranded mRNA library preparation kit (Illumina).

Sequencing of Ribo-seq and RNA-seq libraries were performed in multiplex separately using S1 Flowcell for the NovaSeq 6000 sequencer (Illumina). Demultiplexing was performed using bcl2fastq software (Illumina).

Ribosome Sequencing Analysis

FASTQ files for Ribo-seq reads were trimmed for adaptors (3′*AGATCGGAAGAGCACACGTCTGAACTCCAGTCAC*) using cutadapt (v4.0) and then filtered for rRNA reads by aligning against human18S, 28S, 5S, and 5.8S rRNA sequences using Bowtie2 v2.4.5 and collecting unaligned reads with the "–un" argument. FASTQ files for RNA-seq reads were also trimmed for adaptors (3′AGATCGGAAGAGCACACGTCTGAACTCCAGTCA) using cutadapt (v4.0).

Processed RNA-seq and Riob-seq reads were then aligned to the human genome (hg38 release, Ensembl GTF v108) using STAR (v2.7.10b) with "—quantMode" option enabled. Resulting count matrix was then used for translation efficiency analysis as previously described [66] using DEseq2 v1.36.0 and design argument as "~Condition+SeqType+Condition:SeqType", where Condition was cell state (Cyc, Qui, Etop, IR) and SeqType was Ribo-seq or RNA-seq reads. RPKM analysis was obtained starting from the STAR generated read count matrix and then normalizing each gene tot total reads sequenced obtained from de-multiplexed fastq files prior to alignment; library-normalized reads were then transformed into RPKM by dividing reads by the max annotated transcript length (kb) for each gene.

Treatment of cells with proteotoxic and metabolic stress

Starvation media (-Met -Cys) was prepared from high glucose DMEM lacking glutamine, methionine, and cysteine (Gibco) and then supplemented with 20% dialyzed FBS and glutamine to typical DMEM levels. Amino acid starvation was then performed by removing media from cultured cells, washing once in PBS, and then replacing with -Met -Cys media followed by incubation for 3h unless otherwise indicated. Proteotoxic stress was induced using thapsigargin (Tg, Sigma) supplemented into culture media described previously at 25 nM and incubated on cells for 3 h unless otherwise indicated. Cells for either stress condition were harvested after

484 treatment and then prepared for bulk RNA or protein lysates as described above, or for direct-
485 RNA nanopore sequencing as described below.

486 **Direct-RNA Nanopore sequencing**
487 Total RNAs were extracted from cells grown in 150 mM plates using Trizol according to
488 manufacturer's instructions. RNA quality was measured using a Tapestation gel electrophoresis
489 system (Agilent) and RNA integrity numbers greater than 8 were considered suitable for
490 analysis. RNA was then prepared for sequencing essentially as described for TERA5-Seq [46].
491 Briefly, ~40 µg of bulk RNA was subjected to poly(A) selection using Oligo d(T)25 magnetic
492 beads (NEB) followed by on-bead 5' ligation of a biotinylated REL5 linker sequence using T4
493 RNA ligase 1 (NEB) for 3 h at 37ºC. 500 ng of REL5-ligated polyA RNAs were used for library
494 preparation using the direct RNA sequencing kit (Nanopore Technologies). Libraries were
495 quantified using a Quibit 1X dsDNA High Sensitivity assay kit (ThermoFisher Scientific) and
496 then analyzed on a FLO-MIN106 flow cell on a Minion device (Nanopore Technologies).

497 **Processing and analysis of direct-RNA long-read sequencing**
498 Direct RNA sequencing data were basecalled using Guppy (v3.4.5). By protocol design, some
499 reads contain a 5' linker (REL5) that marks the in-vivo 5' end. Cutadapt (v2.8) was used to
500 identify and remove adaptors ligated on the 5' end of reads using parameters -g
501 AATGATACGGCGACCACCGAGATCTACACTCTTTCCCTACACGACGCTCTTCCGATCT --
502 overlap 31 --minimum-length 25 --error-rate 0. All reads except those smaller than 25nts are
503 retained from further processing. Information about reads containing the adaptor is also retained
504 for targeted analysis of 5' end degradation. All reads were subsequently aligned against
505 ribosomal sequences using minimap2 (v2.17). Reads that matched ribosomal sequences were
506 excluded from further analysis. Filtered reads were mapped on reference human genome build
507 38 (hg38) using minimap2 (v2.17) with parameters -a -x splice -k 12 -u b -p 1 --secondary=yes.
508 They were also aligned against the human transcriptome (Ensembl v91) with parameters -a -x
509 map-ont -k 12 -u f -p 1 --secondary=yes. Transcript count was quantified as the number of
510 reads aligning on each transcript. Differential expression of transcripts/genes was performed
511 with DESeq2[67].

512 **Poly-A tail and transcript length analysis**
513 Nanopolish polya was used to extract poly(A) tail lengths from raw nanopore signal[68]. Only
514 poly(A) tail lengths that passed the software quality control scores and were tagged as "PASS"
515 were used in further analysis. Differential analysis for poly(A) tail and read lengths across
516 conditions was performed with NanopLen package using the linear mixed model option for
517 quantification of statistical significance (https://github.com/maragkakislab/nanoplen). In-house
518 python scripts were used for data visualization.

519 **Transcriptome isoform analysis**
520 Isoform analysis from direct RNA sequencing data was performed using FLAIR [69]. All libraries
521 were merged for isoform identification in order to create a common reference for all downstream
522 comparisons. Differential isoform usage across conditions was then performed with
523 diff_iso_usage.py and diffsplice_fishers_exact.py. Hits that were common in both replicate
524 comparisons were selected as high confidence isoforms.

525 **Transfection of *in vitro* generated mRNA**

526 cDNA for *in-vitro* generated mRNA constructs was obtained from expansion of an ATF4
527 Mammalian Gene Collection *Escherichia Coli* strain (Horizon Gene Editing, Clone ID: 3454473),
528 while G. Extracted DNA was PCR amplified using primers listed in **Table S4** to generate *ATF4*
529 WT or Mut constructs, purified (PCR Cleanup Kit, Qiagen) and mRNA was generated using
530 mMESSAGe mMACHINE T7 Ultra Kit (Ambion) according to manufacturer's instructions. 500
531 ng of generated mRNA was transfected into Cyc or Etop cells using 4 µl Lipofectamine
532 MessengerMAX Reagent (ThermoFisher Scientific). Cells were incubated for 12 hours until
533 harvest for bulk RNA and protein extraction.

534 **Protein synthesis assay**
535 Protein synthesis was measured using the Click-iT HPG Alexa Fluor 488 Protein Synthesis
536 Assay kit (ThermoFisher Scientific). Cells were labeled in media as described above
537 supplemented with 50 µM homo-paraglycine (HPG, methionine analogue) for times indicated in
538 experiments. After labeling, cells were fixed and analyzed as per manufacturer's instructions
539 using a BZ-X (Keyence) fluorescent microscope. Protein synthesis was quantified by extracting
540 the total brightness measured in the blue channel (fluorescein) from areas positive in the DAPI
541 channel.

542 **Polysome profiling**
543 Lysates for polysome profiling were prepared by treating cells with 100 µg/mL cycloheximide
544 (Sigma) in culture media for 10 minutes at 37ºC. Cells were then washed with ice-cold PBS also
545 containing cycloheximide and lysed on ice by adding Polysome Buffer (20 mM Tris pH 7.4, 150
546 mM NaCl, 5 mM $MgCl_2$, 1 mM DTT, 1 % v/v Triton X-100, 1x protease inhibitors (ThermoFisher
547 Sceintific), 20 U/mL DNase I (Roche), 100 µg/mL cycloheximide) dropwise to cells and then
548 scraping. Lysate was then triturated through a 26G needle (BD) and centrifuged for 10 minutes
549 at 20k x g at 4ºC. RNA content was approximated using UV absorbance on a Nanodrop
550 machine and 20 µg of RNA was loaded onto 5%-45% sucrose gradient and analyzed on a
551 UV/VIS fractionator (Brandell). Raw absorbance readings were analyzed and plotted in R and
552 normalized UV absorbance was calculated by dividing each measurement over the total
553 absorbance measured.

Figures

Figure 1

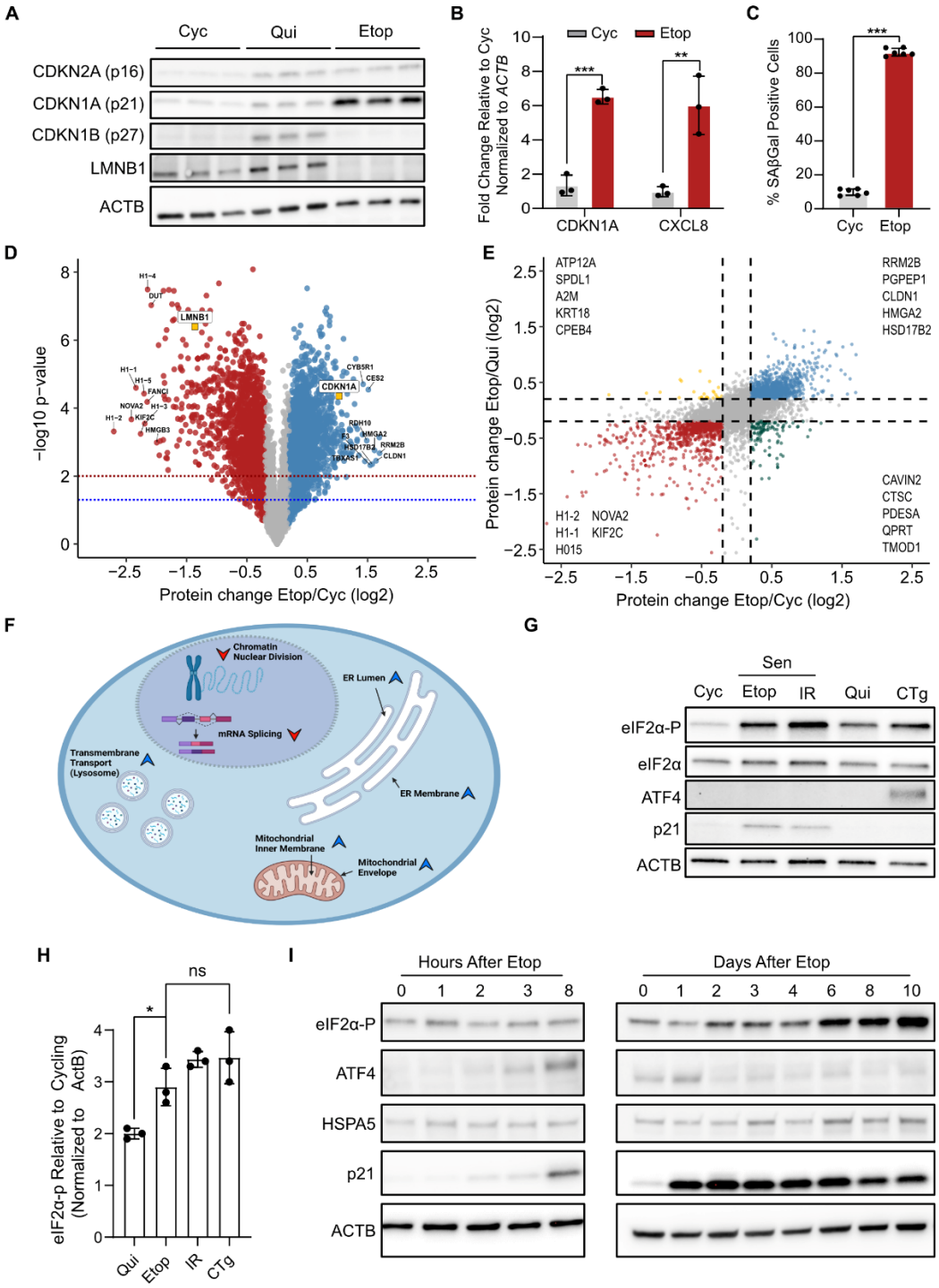

Figure 1. Cellular senescence is characterized by persistent ER stress signaling but no downstream ATF4 activation (A) Western blot analysis of cell cycle arrest markers p21 (CDKN1A), p16 (CDKN2A) and p27 (CDKN1B) and nuclear protein Lamin B1 (LMNB1) for etoposide induced senescent, quiescent, and cycling cells. ACTB is used as control. **(B)** RT-qPCR analysis of *CDKN1A* and *CXCL8* mRNAs from cells analyzed in (A). Significance determed by t-test with n=3 (**= pvalue<0.01; *** = pvalue < 0.001) **(C)** Quantification of beta galactosidase staining (SA-βGal) of etoposide treated and cycling cells (*** = pvalue < 0.001). **(D)** Volcano plot of Etop/Cyc differential protein

562 expression analysis. Statistically significant (p-value ≤ 0.05 by two-tailed t-test) log2FC values are colored as follows:
563 log2FC ≥ 0.2, blue; log2FC ≤ -0.2, red; log2FC between -0.2 and 0.2, grey. **(E)** Scatterplot of protein fold-change
564 values from the Etop/Cyc (x-axis) and Etop/Qui (y-axis) comparisons. Dotted lines mark 0.2 and -0.2 log2FC in both
565 comparisons. Quadrants are annotated with the top 5 most changed proteins, with respect to Etop/Cyc. **(F)** Summary
566 schematic of GSEA for senescence-specific increased and decreased proteins. Red arrows indicate annotation is
567 suppressed in senescence and blue arrows indicate annotation is increased in senescence. **(G)** Western blot analysis
568 of ISR markers eIF2α phosphorylation (eIF2α-P) and ATF4; cells analyzed are cycling (Cyc), etoposide-induced
569 senescent (Etop), ionizing-radiation induced senescent (IR), contact-inhibited quiescent (Qui), and thapsigargin-
570 treated (CTg, 25 nM 3h). **(H)** Quantification of eIF2α-P signal relative to Cyc cells for Etop, IR, Qui, and CTg cells
571 determined from western blot analysis in triplicate; normalized against ACTB protein expression. **(I)** Western blot of
572 lysates harvested at indicated time points after initial etoposide treatment (left, hours; right, days).

573

Figure 2

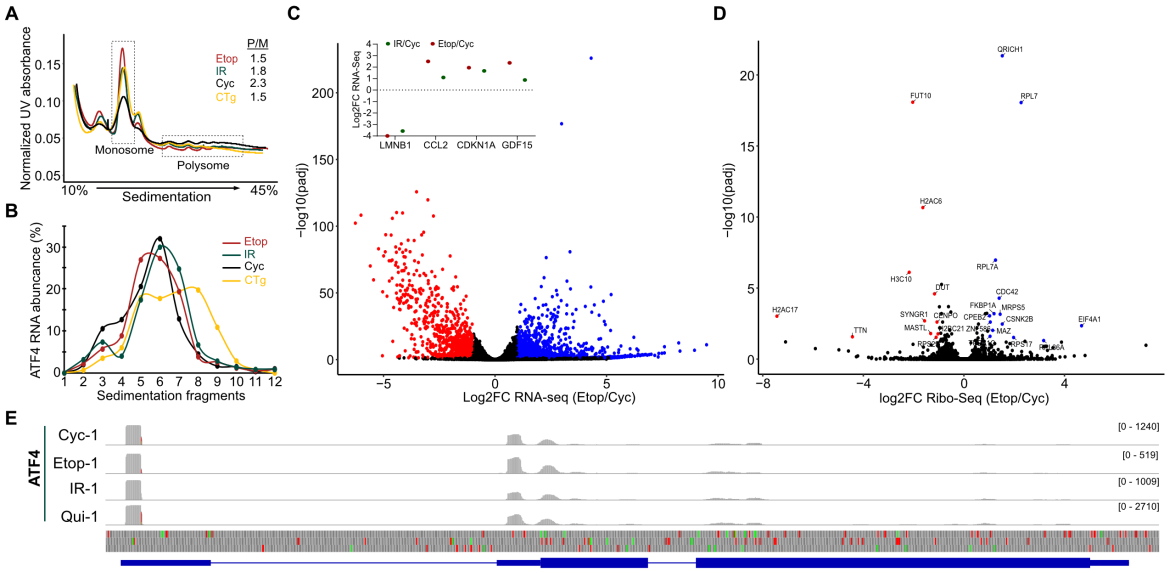

Figure 2. Ribosome sequencing shows that uORF bypass is not activated in senescent cells. (A) Polysome profiling traces on a 10-45% sucrose gradient for lysates from indicated cell types after treatment with 0.1 mg/mL. The ratio of polysome/monosome fractions (P/M) are quantified and shown in inset. **(B)** RT-qPCR analysis of ATF4 levels for RNA extracted from the polysome profiling experiment described above; increasing fragments correspond to higher density sucrose and polysomes. **(C)** Volcano plot of Etop/Cyc differential RNA-seq expression analysis. Statistically significant (adjusted p-value ≤ 0.05 by two-tailed t-test) log2FC values are colored as follows: log2FC ≤ -1, red; log2FC ≥ 1, blue; log2FC between -1 and 1, black. Inset indicates log2FC values for senescence markers in the Etop/Cyc (shown) and IR/Cyc comparisons. **(D)** Volcano plot of Etop/Cyc differential translation efficiency (see methods) from ribosome sequencing. Statistically significant (adjusted p-value ≤ 0.05 by two-tailed t-test) log2FC values are colored as follows: log2FC ≤ -1, red; log2FC ≥ 1, blue; log2FC between -1 and 1, black. **(E)** IGV mapping of Ribo-seq reads for the ATF4 gene locus of the hg38 human genome release. Increased density indicates ribosome occupancy.

Figure 3

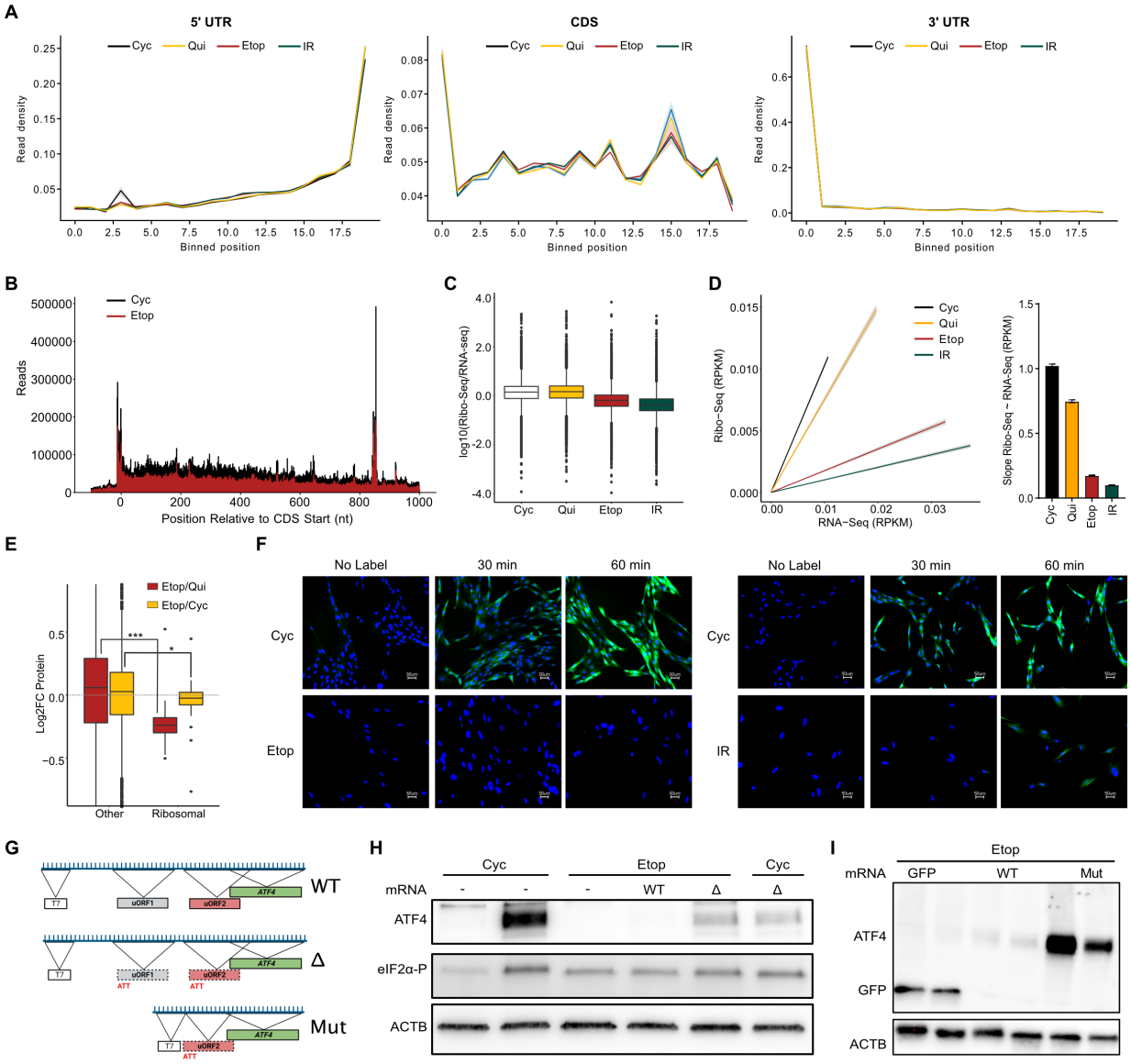

Figure 3. A global decrease in translating ribosomes inhibits the ISR in senescence. (A-B) Metaplot analysis of Ribo-seq reads mapped to the transcriptome. In **(A),** the 5' end coordinates of aligned reads are transformed to binned coordinates that effectively represent percentage of total gene length, and in **(B)**, reads are aligned relative to annotated CDS start sites. **(C)** Boxplot of $\log_{10}$(Ribo-seq/RNA-seq) reads as determined by RPKM analysis (see methods); boxplot inset of the same data with median of each sample marked. **(D)**. Linear regression analysis of Ribo-seq~RNA-seq reads (left) and barplot comparing slopes obtained with standard error (right). **(E)** Boxplot of ribosomal protein (RProtein) abundances from mass spectrometry data for Etop/Cyc (red) and Etop/Qui (yellow) comparisons. The RProtein group is significantly reduced compared to the total group of proteins in each comparison by student's t-test (*= pvalue<0.01; *** = pvalue < 0.001). **(F)** Representative immunofluorescence images (n=4) from Etop and Cyc cells pulsed with 50 μM methionine analogue and fixed after indicated time. **(G)** Diagram of T7-ATF4 mRNA constructs for transfection; dotted lines indicate uORF initiation site has been mutated as shown. **(H-I)** Western blot analysis of transfected T7 transcribed *ATF4* mRNA.

Figure 4

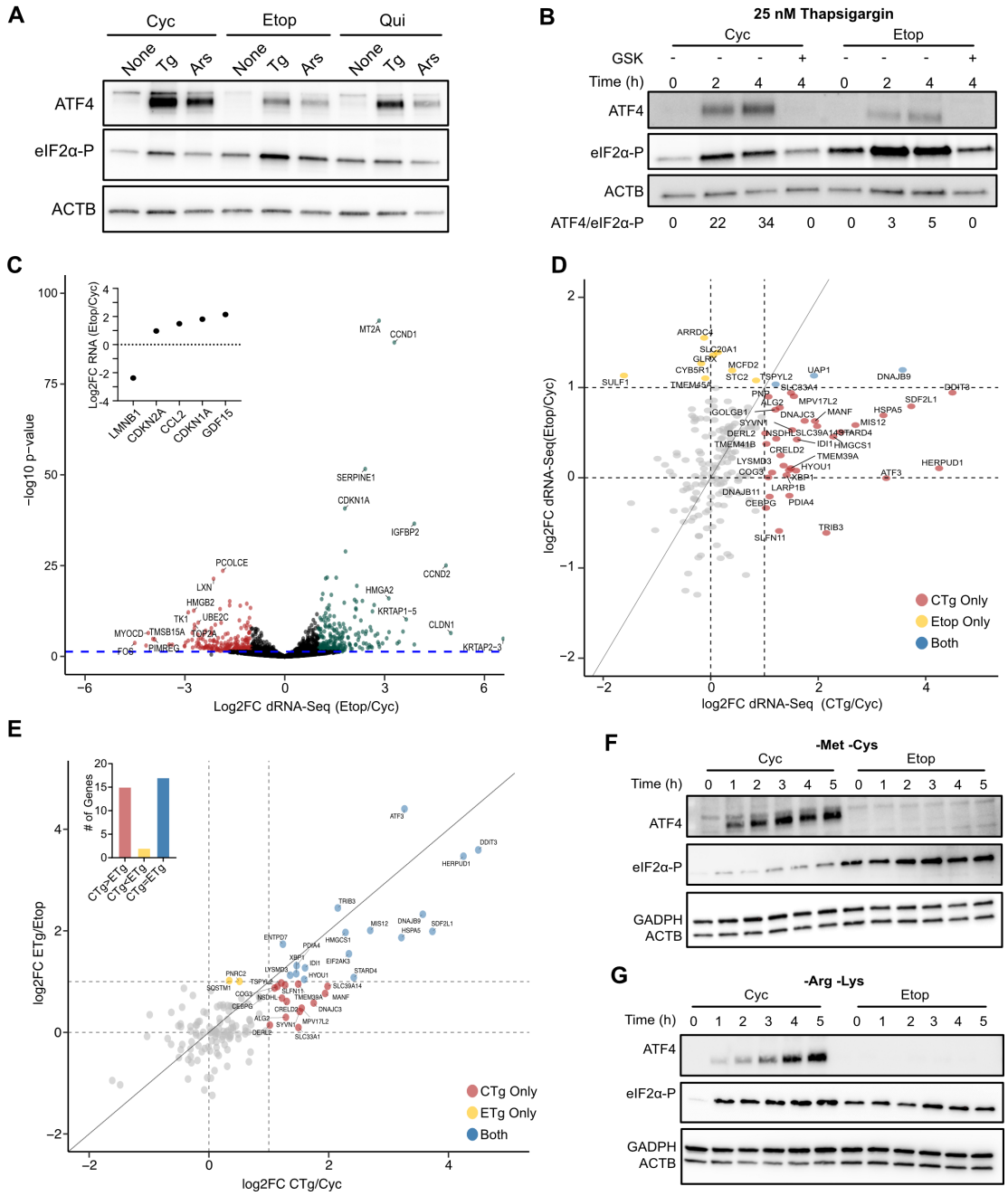

Figure 4. Senescent cells fail to activate the ISR in response to acute stress. (A) Western blot of Etop, Cyc, and Qui cells treated for 3 h with vehicle (none), 25nM Tg (Tg), or 250 μM sodium arsenite (Ars). **(B)** Western blot of Etop and Cyc cells treated with 25 nM Tg and harvested after indicated times; eIF2AK3 inhibitor (GSK, 550 nM) added concurrently with Tg for indicated lane. The ATF4/eIF2α-P ratio is determined by intensity-based quantification and rounded to nearest whole number. **(B)** Western blot of Cyc and Etop cells treated with 25nM thapsigargin for 3h in biological triplicate as indicated. **(C)** Volcano plot of nanopore-based direct RNA sequencing (dRNA-seq) abundance changes for Etop vs. Cyc cells. RNAs with statistically significant (adjusted p-value ≤ 0.05 by two-tailed t-test) abundance increase in red, decrease in green. The top ten genes, increased or decreased, are annotated. **(D-E)** Scatter plot of differential gene expression for previously described ER-stress activated genes[21,47,48]. Dots are colored based on whether they are at least 2-fold increased (above dashed lines) in the indicated comparisons (exclusive or both). For **(E)**, sum of total genes in each category shown as inset. **(F-G)** Western blot of Cyc and Etop

615 cells starved for indicated times in culture media lacking amino acids, for **(F)** Methionine and Cysteine (-Met -Cys)
616 and for **(G)** Arginine and Lysine (-Arg -Lys).
617

Figure 5

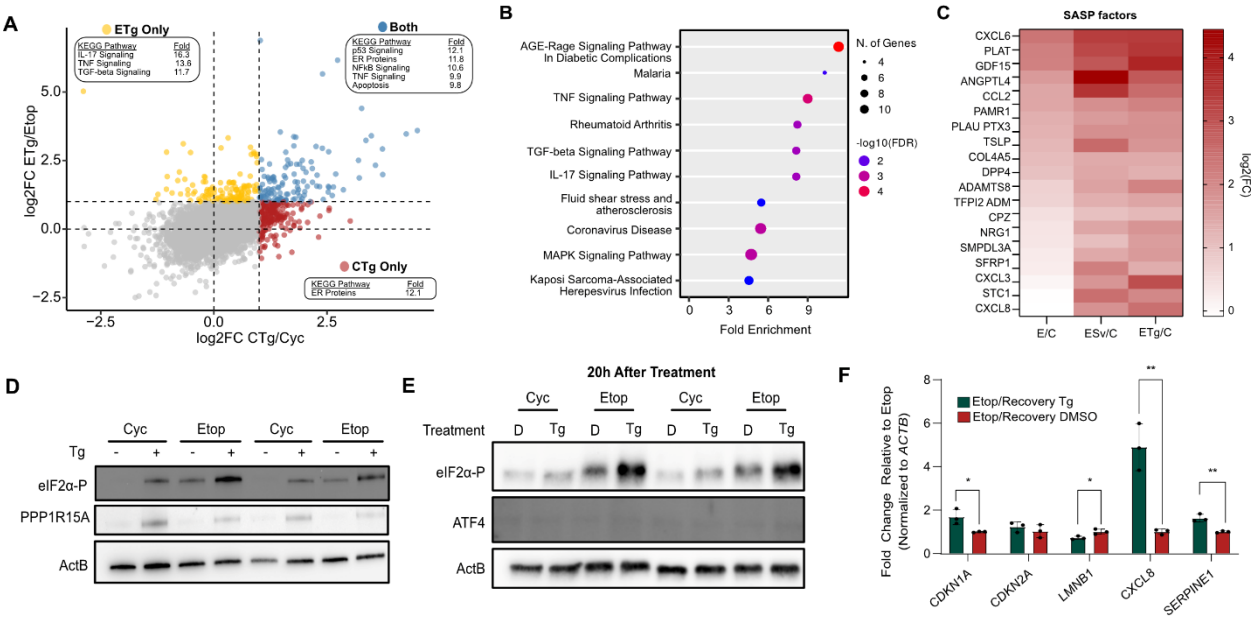

Figure 5. Unresolved acute stress enhances the senescence associated secretory phenotype. (A) Comparison of log2FC values for the ETg/Etop and CTg/Cyc comparisons for all detected RNAs; insets show enriched non-disease KEGG pathways for genes in respective quadrant. **(B)** KEGG pathway enrichment analysis of genes observed to be uniquely enhanced by stress. **(C)** Heatmap of genes with annotated secretory function in the stress enhanced gene set; color indicates increasing log2FC for each library relative to cycling cells. **(D)** Western blot analysis of cells treated with or without thapsigargin (Tg; 25 nM, 3h). **(E)** Western blot of cells treated with DMSO (D) or Tg (as above) and then allowed to recover for 20h before harvest. **(F)** RT-qPCR analysis of cells treated in **(E)**, significance assessed by student's t-test (n=3, *= pvalue<0.01; ** = pvalue < 0.01).

Figure 6

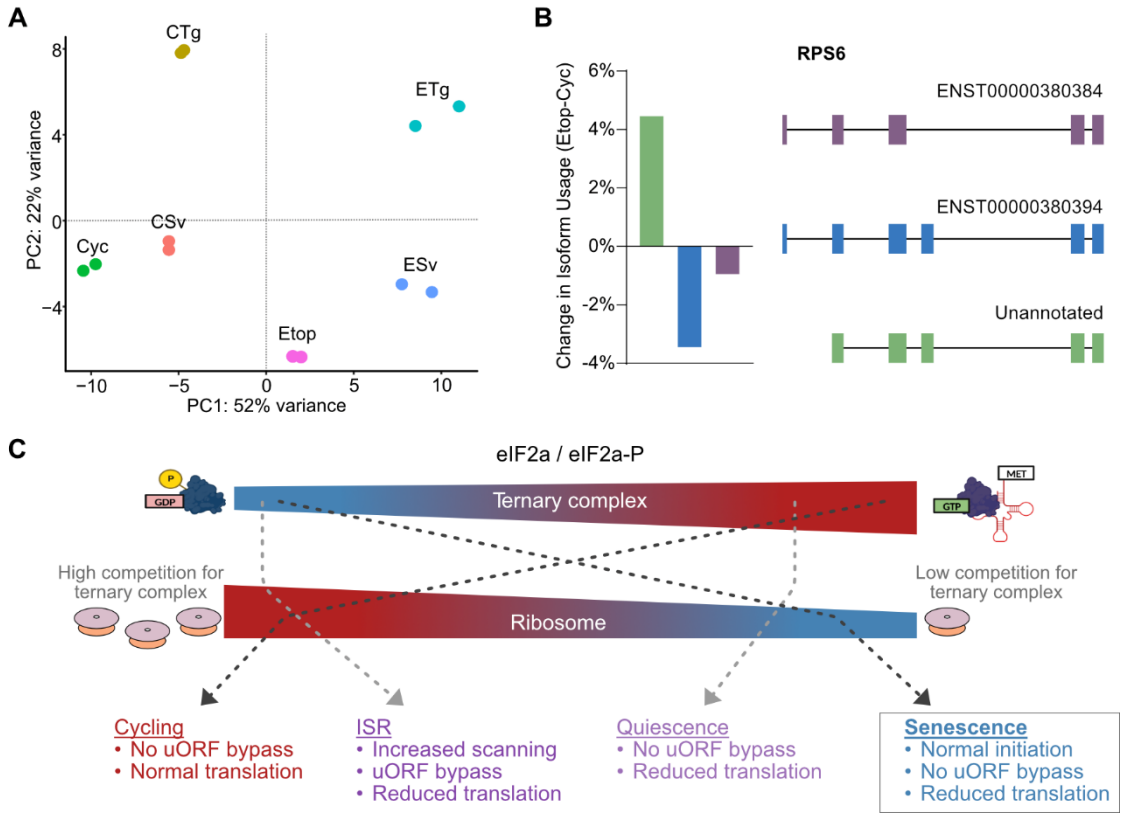

Figure 6. Model for translation repression and ISR inhibition in senescence. (A) Scatter plot of PC1 and PC2 from PCA of dRNA-Seq libraries. **(B)** Barplot of percent change in isoform usage and schematic of isoform structure for RPS6. **(C)** Model of reduced uORF bypass as a consequence of the imbalance of eIF2α/eIF2α-P ratio and ribosome abundance that results in persistent state of stress desensitization.

Figure S1

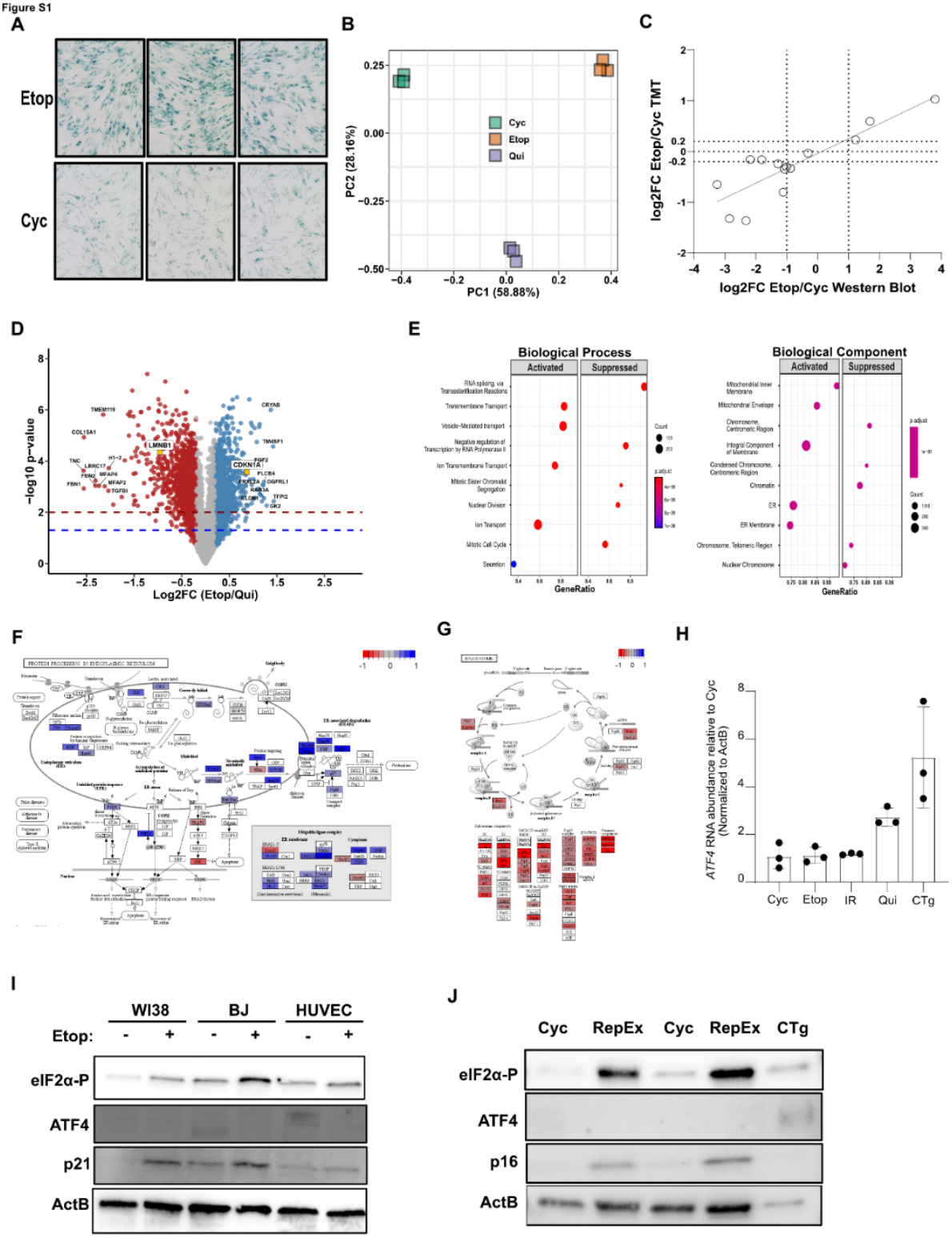
A
Etop
Cyc
B
PC2 (28.16%)
PC1 (58.88%)
Cyc
Etop
Qui
C
log2FC Etop/Cyc TMT
log2FC Etop/Cyc Western Blot
D
−log10 p−value
Log2FC (Etop/Qui)
E
Biological Process
Activated
Suppressed
GeneRatio
Biological Component
Activated
Suppressed
GeneRatio
F
G
H
ATF4 RNA abundance relative to Cyc (Normalized to ActB)
Cyc
Etop
IR
Qui
CTg
I
WI38
BJ
HUVEC
Etop:
eIF2α-P
ATF4
p21
ActB
J
Cyc
RepEx
Cyc
RepEx
CTg
eIF2α-P
ATF4
p16
ActB

Figure S1. (A) Representative brightfield microscopy images of senescence-associated beta-galactosidase assay (n=6). **(B)** Principal component analysis of mass spectrometry data **(Table S1)**; boxes represent individual replicates for each cell state (n=3). **(C)** Correlation of log2FC measured by mass spectrometry and western blot analysis after normalization to ACTB for selected proteins (RPS20, p21, PCNA, LMNB1, eIF5, eIF2α, RPS10, eEF2, eEF2K, HSPA5, $p16^{INK4A}$, RPL14, eEF1A, eIF4EBP1). Dashed lines on y-axis correspond to cutoff used to determine substantial change in mass spectrometry data, dashed lines on x-axis correspond to log2FC of 1/-1. **(D)** Volcano plot of Etop/Qui differential protein expression analysis. Statistically significant (p-value ≤ 0.05 by two-tailed t-test) log2FC values are colored as follows: log2FC ≥ 0.2, blue; log2FC ≤ -0.2, red; log2FC between -0.2 and 0.2, grey. **(E)** Gene set enrichment analysis (GSEA) of proteins with uniquely increased and decreased expression in senescence. GSEA was performed for annotations in biological process (left) and cellular component (right) and p-value cutoff of 0.05. **(F-G)** KEGG pathway analysis of uniquely increased or decreased proteins visualized using Pathview[70]. Color indicates log2FC from mass spectrometry analysis. **(H)** RT-qPCR analysis for *ATF4* in indicated cell states (n=3). **(I)** Western blot analysis of Etop induced senescence in three additional cell types: WI-38 lung fibroblasts (WI38, 50μM etoposide), BJ human foreskin fibroblasts (BJ, 25μM etoposide), and Human Vein Endothelial Cells (HUVEC, 10μM etoposide). **(J)** Western blot analysis of replicative exhaustion induced senescent (RepEx) cells (PDL ~60).

Figure S2

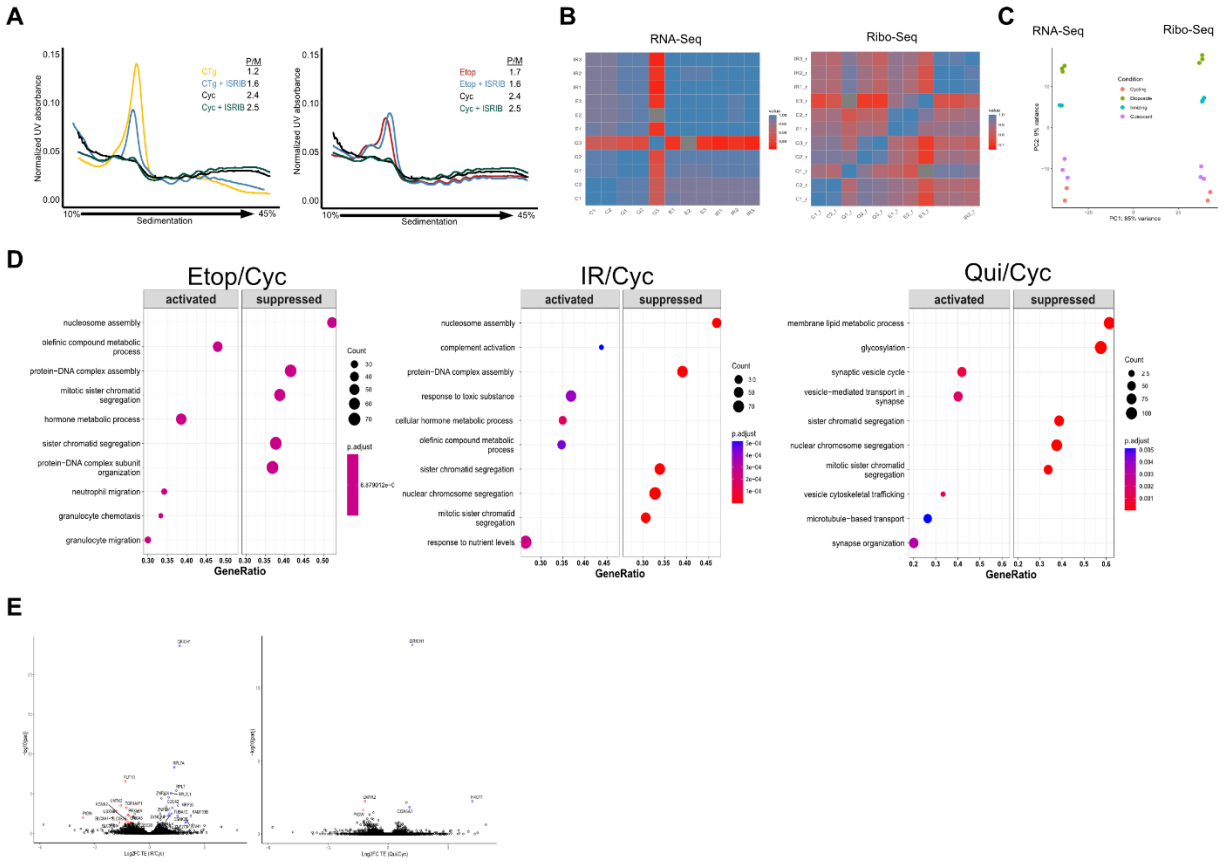

Figure S2. (A) Polysome profiling of cells treated with Tg (25 nM, 3h), ISRIB (10 nM, 24h) , or both. Translation rate assessed by polysome/monosome ratio (P/M). **(B)** Correlogram of RNA-seq and Ribo-seq libraries. **(C)** PCA of RNA-seq and Ribo-seq libraries; colors indicate cell type. **(D)** GSEA for biological process from RNA-seq data of indicated comparisons. **(E)** Volcano plot of differential translation efficiency for IR/Cyc (left) and Qui/Cyc (right) from ribosome sequencing. Statistically significant (adjusted p-value ≤ 0.05 by two-tailed t-test) log2FC values are colored as follows: log2FC ≤ -1, red; log2FC ≥ 1, blue; log2FC between -1 and 1, black.

Figure S3

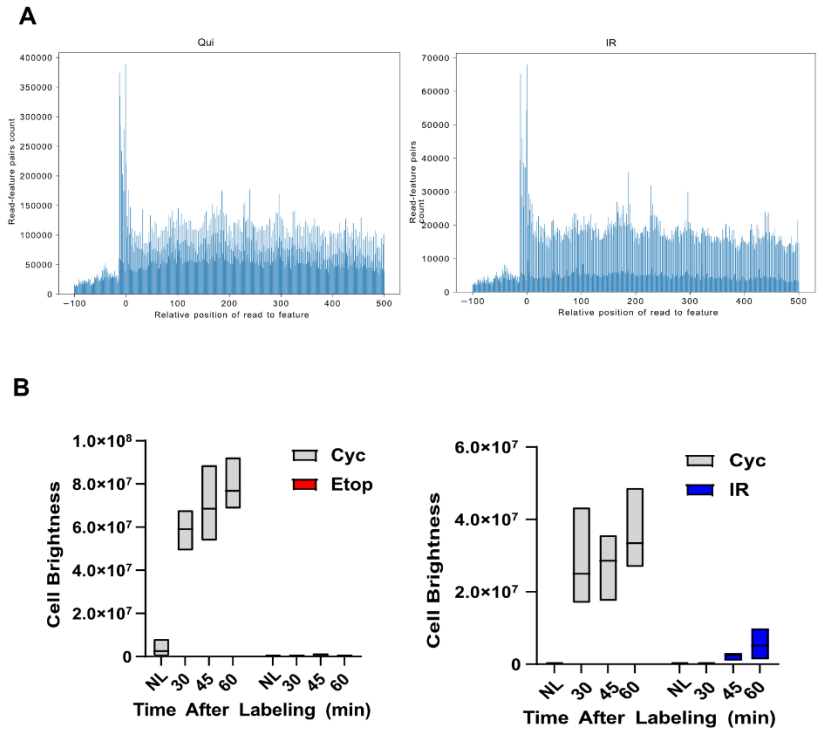

Figure S3. (A) Metaplot analysis of Ribo-seq reads mapped to the transcriptome. Reads are aligned relative to annotated CDS start sites and are not normalized to gene length (positions are true nucleotide distances).

Figure S4

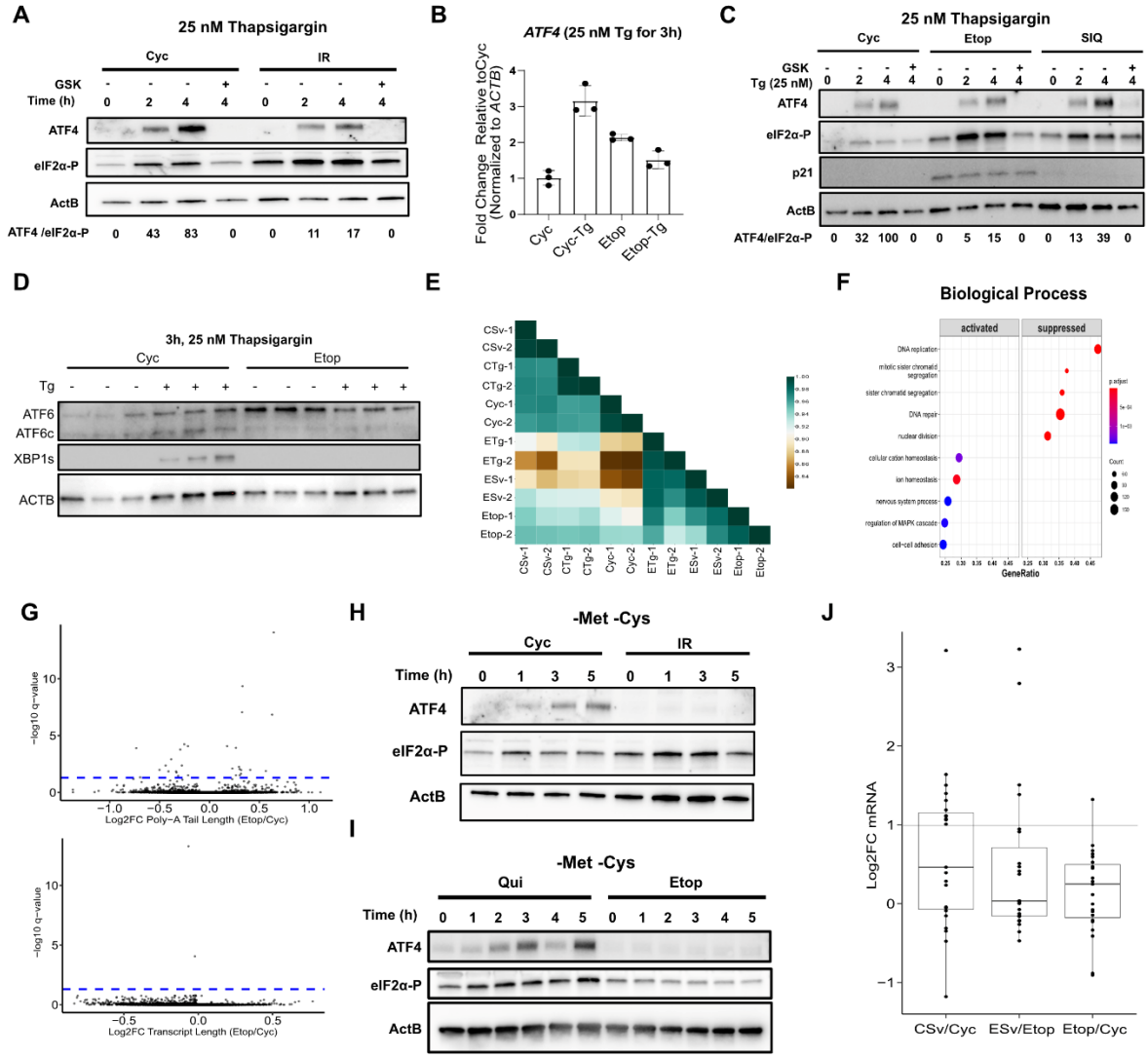

Figure S4. (A) Western blot analysis of Cyc and IR cells treated with 25 nM Tg at indicated times. ATF4/eIF2α-P ratio calculated using densiometric analysis of shown western blots and rounded to nearest integer; GSK (550 nM) added concurrently with Tg for indicated lanes. **(B)** RT-qPCR analysis for *ATF4* mRNA from bulk RNA extracted from Etop and Cyc cells with and without Tg treatment (3h, 25 nM). **(C)** Western blot analysis of Cyc, Etop and serum-induced quiescent (SIQ) cells treated with 25 nM for indicated times; GSK (550 nM) added concurrently with Tg for indicated lanes. SIQ cells were prepared by growing cells in media with 0.2% FBS for 10d. **(D)** Western blot analysis of Cyc and Etop cells treated with 250 ng/mL tunicamycin (Tm) for indicated times ; GSK (550 nM) added concurrently with (Tm) for indicated lanes. **(E)** Correlogram of dRNA-seq libraries. **(F)** GSEA for biological process of dRNA-seq Etop/Cyc comparison. **(G)** Volcano plots of log2 fold change for poly-A tail length (top) and transcript length (bottom) for Etop/Cyc dRNA-seq libraries obtained from NanopLen analysis (see methods). **(H-I)** Western blot analysis after starvation of methionine and cysteine amino acids cultured for indicated times. **(J)** Boxplot of dRNA-seq analysis for starvation genes[49]

Data availability

Sequencing data have been deposited in the Sequence Read Archive (SRA); accession: GSE223762 and GSE227766. Raw mass spectrometry data are available at the MassIVE data repository; accession: MSV000091077.

Acknowledgements

This research was supported by the Intramural Research Program of the National Institute on Aging, National Institutes of Health (ZIAAG000696).

Author contributions

MJP performed wet-lab experiments with assistance from JM, RM, CA, CB, JF, YP, SM, LW, and KA. SD performed computational analysis on dRNA-seq data. MJP performed computational analysis on mass spectrometry data and ribosome sequencing data. MJP and MM interpreted the data assisted by AR, NB and MG. MJP and MM wrote the manuscript with feedback from all authors.

References

1 Rodier, F. & Campisi, J. Four faces of cellular senescence. *J Cell Biol* **192**, 547-556, doi:10.1083/jcb.201009094 (2011).

2 Lowe, S. W., Cepero, E. & Evan, G. Intrinsic tumour suppression. *Nature* **432**, 307-315, doi:10.1038/nature03098 (2004).

3 Munoz-Espin, D. *et al.* Programmed cell senescence during mammalian embryonic development. *Cell* **155**, 1104-1118, doi:10.1016/j.cell.2013.10.019 (2013).

4 Demaria, M. *et al.* An essential role for senescent cells in optimal wound healing through secretion of PDGF-AA. *Dev Cell* **31**, 722-733, doi:10.1016/j.devcel.2014.11.012 (2014).

5 Wilkinson, H. N. & Hardman, M. J. Cellular Senescence in Acute and Chronic Wound Repair. *Cold Spring Harb Perspect Biol*, doi:10.1101/cshperspect.a041221 (2022).

6 Tuttle, C. S. L. *et al.* Cellular senescence and chronological age in various human tissues: A systematic review and meta-analysis. *Aging Cell* **19**, e13083, doi:10.1111/acel.13083 (2020).

7 Rouault, C. *et al.* Senescence-associated beta-galactosidase in subcutaneous adipose tissue associates with altered glycaemic status and truncal fat in severe obesity. *Diabetologia* **64**, 240-254, doi:10.1007/s00125-020-05307-0 (2021).

8 Shorter, E. *et al.* Identifying Novel Osteoarthritis-Associated Genes in Human Cartilage Using a Systematic Meta-Analysis and a Multi-Source Integrated Network. *Int J Mol Sci* **23**, doi:10.3390/ijms23084395 (2022).

9 Bussian, T. J. *et al.* Clearance of senescent glial cells prevents tau-dependent pathology and cognitive decline. *Nature* **562**, 578-582, doi:10.1038/s41586-018-0543-y (2018).

720 10 Coppe, J. P. *et al.* Senescence-associated secretory phenotypes reveal cell-nonautonomous
721 functions of oncogenic RAS and the p53 tumor suppressor. *PLoS Biol* **6**, 2853-2868,
722 doi:10.1371/journal.pbio.0060301 (2008).
723 11 Basisty, N. *et al.* A proteomic atlas of senescence-associated secretomes for aging biomarker
724 development. *PLoS Biol* **18**, e3000599, doi:10.1371/journal.pbio.3000599 (2020).
725 12 Acosta, J. C. *et al.* A complex secretory program orchestrated by the inflammasome controls
726 paracrine senescence. *Nat Cell Biol* **15**, 978-990, doi:10.1038/ncb2784 (2013).
727 13 Coppe, J. P., Desprez, P. Y., Krtolica, A. & Campisi, J. The senescence-associated secretory
728 phenotype: the dark side of tumor suppression. *Annu Rev Pathol* **5**, 99-118,
729 doi:10.1146/annurev-pathol-121808-102144 (2010).
730 14 Franceschi, C. & Campisi, J. Chronic inflammation (inflammaging) and its potential contribution
731 to age-associated diseases. *J Gerontol A Biol Sci Med Sci* **69 Suppl 1**, S4-9,
732 doi:10.1093/gerona/glu057 (2014).
733 15 Justice, J. N. *et al.* Senolytics in idiopathic pulmonary fibrosis: Results from a first-in-human,
734 open-label, pilot study. *EBioMedicine* **40**, 554-563, doi:10.1016/j.ebiom.2018.12.052 (2019).
735 16 Xu, M. *et al.* Senolytics improve physical function and increase lifespan in old age. *Nat Med* **24**,
736 1246-1256, doi:10.1038/s41591-018-0092-9 (2018).
737 17 Cai, Y. *et al.* Elimination of senescent cells by beta-galactosidase-targeted prodrug attenuates
738 inflammation and restores physical function in aged mice. *Cell Res* **30**, 574-589,
739 doi:10.1038/s41422-020-0314-9 (2020).
740 18 Borghesan, M., Hoogaars, W. M. H., Varela-Eirin, M., Talma, N. & Demaria, M. A Senescence-
741 Centric View of Aging: Implications for Longevity and Disease. *Trends Cell Biol* **30**, 777-791,
742 doi:10.1016/j.tcb.2020.07.002 (2020).
743 19 Dorr, J. R. *et al.* Synthetic lethal metabolic targeting of cellular senescence in cancer therapy.
744 *Nature* **501**, 421-425, doi:10.1038/nature12437 (2013).
745 20 Pakos-Zebrucka, K. *et al.* The integrated stress response. *EMBO Rep* **17**, 1374-1395,
746 doi:10.15252/embr.201642195 (2016).
747 21 Han, J. *et al.* ER-stress-induced transcriptional regulation increases protein synthesis leading to
748 cell death. *Nat Cell Biol* **15**, 481-490, doi:10.1038/ncb2738 (2013).
749 22 Wortel, I. M. N., van der Meer, L. T., Kilberg, M. S. & van Leeuwen, F. N. Surviving Stress:
750 Modulation of ATF4-Mediated Stress Responses in Normal and Malignant Cells. *Trends*
751 *Endocrinol Metab* **28**, 794-806, doi:10.1016/j.tem.2017.07.003 (2017).
752 23 Sabath, N. *et al.* Cellular proteostasis decline in human senescence. *Proc Natl Acad Sci U S A* **117**,
753 31902-31913, doi:10.1073/pnas.2018138117 (2020).
754 24 Hernandez-Segura, A. *et al.* Unmasking Transcriptional Heterogeneity in Senescent Cells. *Curr*
755 *Biol* **27**, 2652-2660 e2654, doi:10.1016/j.cub.2017.07.033 (2017).
756 25 Casella, G. *et al.* Transcriptome signature of cellular senescence. *Nucleic Acids Res* **47**, 7294-
757 7305, doi:10.1093/nar/gkz555 (2019).
758 26 Waldera-Lupa, D. M. *et al.* Proteome-wide analysis reveals an age-associated cellular phenotype
759 of in situ aged human fibroblasts. *Aging (Albany NY)* **6**, 856-878, doi:10.18632/aging.100698
760 (2014).
761 27 Flor, A. C., Wolfgeher, D., Wu, D. & Kron, S. J. A signature of enhanced lipid metabolism, lipid
762 peroxidation and aldehyde stress in therapy-induced senescence. *Cell Death Discov* **3**, 17075,
763 doi:10.1038/cddiscovery.2017.75 (2017).
764 28 Delfarah, A., Hartel, N. G., Zheng, D., Yang, J. & Graham, N. A. Identification of a Proteomic
765 Signature of Senescence in Primary Human Mammary Epithelial Cells. *J Proteome Res* **20**, 5169-
766 5179, doi:10.1021/acs.jproteome.1c00659 (2021).

767 29 Payea, M. J., Anerillas, C., Tharakan, R. & Gorospe, M. Translational Control during Cellular
768 Senescence. *Mol Cell Biol* **41**, doi:10.1128/MCB.00512-20 (2021).
769 30 Anerillas, C. *et al.* Early SRC activation skews cell fate from apoptosis to senescence. *Sci Adv* **8**,
770 eabm0756, doi:10.1126/sciadv.abm0756 (2022).
771 31 Narita, M. *et al.* Spatial coupling of mTOR and autophagy augments secretory phenotypes.
772 *Science* **332**, 966-970, doi:10.1126/science.1205407 (2011).
773 32 Gorgoulis, V. *et al.* Cellular Senescence: Defining a Path Forward. *Cell* **179**, 813-827,
774 doi:10.1016/j.cell.2019.10.005 (2019).
775 33 Wu, T. *et al.* clusterProfiler 4.0: A universal enrichment tool for interpreting omics data.
776 *Innovation (Camb)* **2**, 100141, doi:10.1016/j.xinn.2021.100141 (2021).
777 34 Kanehisa, M., Furumichi, M., Sato, Y., Kawashima, M. & Ishiguro-Watanabe, M. KEGG for
778 taxonomy-based analysis of pathways and genomes. *Nucleic Acids Res* **51**, D587-D592,
779 doi:10.1093/nar/gkac963 (2023).
780 35 Rutkowski, D. T. *et al.* Adaptation to ER stress is mediated by differential stabilities of pro-
781 survival and pro-apoptotic mRNAs and proteins. *PLoS Biol* **4**, e374,
782 doi:10.1371/journal.pbio.0040374 (2006).
783 36 Dey, S. *et al.* Both transcriptional regulation and translational control of ATF4 are central to the
784 integrated stress response. *J Biol Chem* **285**, 33165-33174, doi:10.1074/jbc.M110.167213
785 (2010).
786 37 Dey, S. *et al.* Transcriptional repression of ATF4 gene by CCAAT/enhancer-binding protein beta
787 (C/EBPbeta) differentially regulates integrated stress response. *J Biol Chem* **287**, 21936-21949,
788 doi:10.1074/jbc.M112.351783 (2012).
789 38 Young, A. R. *et al.* Autophagy mediates the mitotic senescence transition. *Genes Dev* **23**, 798-
790 803, doi:10.1101/gad.519709 (2009).
791 39 Young, S. K. & Wek, R. C. Upstream Open Reading Frames Differentially Regulate Gene-specific
792 Translation in the Integrated Stress Response. *J Biol Chem* **291**, 16927-16935,
793 doi:10.1074/jbc.R116.733899 (2016).
794 40 McGlincy, N. J. & Ingolia, N. T. Transcriptome-wide measurement of translation by ribosome
795 profiling. *Methods* **126**, 112-129, doi:10.1016/j.ymeth.2017.05.028 (2017).
796 41 Lessard, F. *et al.* Senescence-associated ribosome biogenesis defects contributes to cell cycle
797 arrest through the Rb pathway. *Nat Cell Biol* **20**, 789-799, doi:10.1038/s41556-018-0127-y
798 (2018).
799 42 Nishimura, K. *et al.* Perturbation of ribosome biogenesis drives cells into senescence through 5S
800 RNP-mediated p53 activation. *Cell Rep* **10**, 1310-1323, doi:10.1016/j.celrep.2015.01.055 (2015).
801 43 Firczuk, H. *et al.* An in vivo control map for the eukaryotic mRNA translation machinery. *Mol Syst*
802 *Biol* **9**, 635, doi:10.1038/msb.2012.73 (2013).
803 44 Atkins, C. *et al.* Characterization of a novel PERK kinase inhibitor with antitumor and
804 antiangiogenic activity. *Cancer Res* **73**, 1993-2002, doi:10.1158/0008-5472.CAN-12-3109 (2013).
805 45 Walter, P. & Ron, D. The unfolded protein response: from stress pathway to homeostatic
806 regulation. *Science* **334**, 1081-1086, doi:10.1126/science.1209038 (2011).
807 46 Ibrahim, F., Oppelt, J., Maragkakis, M. & Mourelatos, Z. TERA-Seq: true end-to-end sequencing
808 of native RNA molecules for transcriptome characterization. *Nucleic Acids Res* **49**, e115,
809 doi:10.1093/nar/gkab713 (2021).
810 47 Shoulders, M. D. *et al.* Stress-independent activation of XBP1s and/or ATF6 reveals three
811 functionally diverse ER proteostasis environments. *Cell Rep* **3**, 1279-1292,
812 doi:10.1016/j.celrep.2013.03.024 (2013).
813 48 Guan, B. J. *et al.* A Unique ISR Program Determines Cellular Responses to Chronic Stress. *Mol*
814 *Cell* **68**, 885-900 e886, doi:10.1016/j.molcel.2017.11.007 (2017).

49 Tang, X. *et al.* Comprehensive profiling of amino acid response uncovers unique methionine-deprived response dependent on intact creatine biosynthesis. *PLoS Genet* **11**, e1005158, doi:10.1371/journal.pgen.1005158 (2015).
50 Lerner, A. G. *et al.* IRE1alpha induces thioredoxin-interacting protein to activate the NLRP3 inflammasome and promote programmed cell death under irremediable ER stress. *Cell Metab* **16**, 250-264, doi:10.1016/j.cmet.2012.07.007 (2012).
51 Kim, K. H. & Lee, M. S. GDF15 as a central mediator for integrated stress response and a promising therapeutic molecule for metabolic disorders and NASH. *Biochim Biophys Acta Gen Subj* **1865**, 129834, doi:10.1016/j.bbagen.2020.129834 (2021).
52 Santarelli, R. *et al.* KSHV dysregulates bulk macroautophagy, mitophagy and UPR to promote endothelial to mesenchymal transition and CCL2 release, key events in viral-driven sarcomagenesis. *Int J Cancer* **147**, 3500-3510, doi:10.1002/ijc.33163 (2020).
53 Uhlen, M. *et al.* Proteomics. Tissue-based map of the human proteome. *Science* **347**, 1260419, doi:10.1126/science.1260419 (2015).
54 Kuilman, T., Michaloglou, C., Mooi, W. J. & Peeper, D. S. The essence of senescence. *Genes Dev* **24**, 2463-2479, doi:10.1101/gad.1971610 (2010).
55 Da Costa, L. M., Marie, I. & Leblanc, T. M. Diamond-Blackfan anemia. *Hematology Am Soc Hematol Educ Program* **2021**, 353-360, doi:10.1182/hematology.2021000314 (2021).
56 Neurohr, G. E. *et al.* Excessive Cell Growth Causes Cytoplasm Dilution And Contributes to Senescence. *Cell* **176**, 1083-1097 e1018, doi:10.1016/j.cell.2019.01.018 (2019).
57 Wells, J. N. *et al.* Structure and function of yeast Lso2 and human CCDC124 bound to hibernating ribosomes. *PLoS Biol* **18**, e3000780, doi:10.1371/journal.pbio.3000780 (2020).
58 Gemmer, M. *et al.* Visualization of translation and protein biogenesis at the ER membrane. *Nature* **614**, 160-167, doi:10.1038/s41586-022-05638-5 (2023).
59 Smith, P. R. *et al.* Functionally distinct roles for eEF2K in the control of ribosome availability and p-body abundance. *Nat Commun* **12**, 6789, doi:10.1038/s41467-021-27160-4 (2021).
60 Marescal, O. & Cheeseman, I. M. Cellular Mechanisms and Regulation of Quiescence. *Dev Cell* **55**, 259-271, doi:10.1016/j.devcel.2020.09.029 (2020).
61 Herranz, N. *et al.* mTOR regulates MAPKAPK2 translation to control the senescence-associated secretory phenotype. *Nat Cell Biol* **17**, 1205-1217, doi:10.1038/ncb3225 (2015).
62 Alspach, E. *et al.* p38MAPK plays a crucial role in stromal-mediated tumorigenesis. *Cancer Discov* **4**, 716-729, doi:10.1158/2159-8290.CD-13-0743 (2014).
63 Lee, S. *et al.* A post-transcriptional program of chemoresistance by AU-rich elements and TTP in quiescent leukemic cells. *Genome Biol* **21**, 33, doi:10.1186/s13059-020-1936-4 (2020).
64 Mitra, M., Ho, L. D. & Coller, H. A. An In Vitro Model of Cellular Quiescence in Primary Human Dermal Fibroblasts. *Methods Mol Biol* **1686**, 27-47, doi:10.1007/978-1-4939-7371-2_2 (2018).
65 Neri, F., Basisty, N., Desprez, P. Y., Campisi, J. & Schilling, B. Quantitative Proteomic Analysis of the Senescence-Associated Secretory Phenotype by Data-Independent Acquisition. *Curr Protoc* **1**, e32, doi:10.1002/cpz1.32 (2021).
66 Chothani, S. *et al.* deltaTE: Detection of Translationally Regulated Genes by Integrative Analysis of Ribo-seq and RNA-seq Data. *Curr Protoc Mol Biol* **129**, e108, doi:10.1002/cpmb.108 (2019).
67 Love, M. I., Huber, W. & Anders, S. Moderated estimation of fold change and dispersion for RNA-seq data with DESeq2. *Genome Biol* **15**, 550, doi:10.1186/s13059-014-0550-8 (2014).
68 Workman, R. E. *et al.* Nanopore native RNA sequencing of a human poly(A) transcriptome. *Nat Methods* **16**, 1297-1305, doi:10.1038/s41592-019-0617-2 (2019).
69 Tang, A. D. *et al.* Full-length transcript characterization of SF3B1 mutation in chronic lymphocytic leukemia reveals downregulation of retained introns. *Nat Commun* **11**, 1438, doi:10.1038/s41467-020-15171-6 (2020).

70 Luo, W. & Brouwer, C. Pathview: an R/Bioconductor package for pathway-based data integration and visualization. *Bioinformatics* **29**, 1830-1831, doi:10.1093/bioinformatics/btt285 (2013).